A&A 676, A90 (2023)
https://doi.org/10.1051/0004-6361/202245564

Astronomy & Astrophysics

The GAPS programme at TNG

XLIV. Projected rotational velocities of 273 exoplanet-host stars observed with HARPS-N⋆,⋆⋆

M. Rainer[1], S. Desidera[2], F. Borsa[1], D. Barbato[3,4], K. Biazzo[5], A. Bonomo[3], R. Gratton[2], S. Messina[6], G. Scandariato[6], L. Affer[7], S. Benatti[7], I. Carleo[8], L. Cabona[2], E. Covino[9], A. F. Lanza[6], R. Ligi[10], J. Maldonado[7], L. Mancini[11,3,12], D. Nardiello[2,13], D. Sicilia[6], A. Sozzetti[3], A. Bignamini[14], R. Cosentino[15], C. Knapic[14], A. F. Martínez Fiorenzano[15], E. Molinari[16], M. Pedani[15], and E. Poretti[1,15]

(Affiliations can be found after the references)

Received 28 November 2022 / Accepted 22 June 2023

ABSTRACT

Context. The leading spectrographs used for exoplanets' search and characterization offer online data reduction softwares (DRS) that yield, as an ancillary result, the full-width at half-maximum (FWHM) of the cross-correlation function (CCF) that is used to estimate the radial velocity of the host star. The FWHM also contains information on the stellar projected rotational velocity $v_{\rm eq} \sin i_\star$, if appropriately calibrated.

Aims. We wanted to establish a simple relationship to derive the $v_{\rm eq} \sin i_\star$ directly from the FWHM computed by the HARPS-N DRS in the case of slow-rotating solar-like stars. This may also help to recover the stellar inclination $i_\star$, which in turn affects the exoplanets' parameters.

Methods. We selected stars with an inclination of the spin axis compatible with 90 deg by looking at exoplanetary transiting systems with known small sky-projected obliquity: for these calibrators, we can presume that $v_{\rm eq} \sin i_\star$ is equal to stellar equatorial velocity $v_{\rm eq}$. We derived their rotational periods from photometric and spectroscopic time series and their radii from the spectral energy distribution (SED) fitting. This allowed us to recover their $v_{\rm eq}$, which could be compared to the FWHM values of the CCFs obtained both with G2 and K5 spectral-type masks.

Results. We obtained an empirical relation for each mask: this can be used to derive $v_{\rm eq} \sin i_\star$ directly from FWHM values for slow rotators ($FWHM < 20$ km s^{-1}). We applied our relations to 273 exoplanet-host stars observed with HARPS-N, obtaining homogeneous $v_{\rm eq} \sin i_\star$ measurements. When possible, we compared our results with the literature ones to confirm the reliability of our work. We were also able to recover or constrain $i_\star$ for 12 objects with no prior $v_{\rm eq} \sin i_\star$ estimation.

Conclusions. We provide two simple empirical relations to directly convert the HARPS-N FWHM obtained with the G2 and K5 mask to a $v_{\rm eq} \sin i_\star$ value. We tested our results on a statistically significant sample, and we found a good agreement with literature values found with more sophisticated methods for stars with $\log g > 3.5$. We also tried our relation on HARPS and SOPHIE data, and we conclude that it can be used as it is also on FWHM derived by HARPS DRS with the G2 and K5 mask, and it may be adapted to the SOPHIE data as long as the spectra are taken in high-resolution mode.

Key words. planetary systems – techniques: spectroscopic – stars: rotation

1. Introduction

Stable, high-resolution (HR) optical spectrographs are some of the leading instruments used for the search and characterization of the exoplanets: many of them are designed expressly for these studies (e.g. HARPS, HARPS-N, ESPRESSO), and as such they are equipped with dedicated data reduction softwares (DRS). One of the main deliverables of the DRS is the cross-correlation function (CCF) of the reduced spectra with a stellar mask chosen from the available library of spectral-type templates (Baranne et al. 1996; Pepe et al. 2002).

The CCF allows for the radial velocity of the host star to be computed with a very high precision, and it also yields a number of additional parameters, such as the CCF's bisector span (which can be used as an activity indicator), the CCF's contrast, and the full-width at half-maximum (FWHM). The latter may be related to the stellar projected rotational velocity $v_{\rm eq} \sin i_\star$ if appropriately calibrated: in this paper, we present the work done to calibrate the FWHM of the CCF that was computed by the HARPS-N DRS (Cosentino et al. 2014) using the G2 and K5 stellar masks. HARPS-N is the HR optical spectrograph installed at the Telescopio Nazionale *Galileo* (TNG) at the Roque de Los Muchachos Observatory (La Palma, Canary Islands, Spain).

The use of the CCF's FWHM to estimate the $v_{\rm eq} \sin i_\star$ is particularly important in the case of slowly rotating stars, for which the $v_{\rm eq} \sin i_\star$ computation via Fourier transform of the line profiles or fitting with a rotational profile is complicated by the combination of rotational broadening with the effects of resolution smearing (≈2.6 km s^{-1} in the case of HARPS-N,

⋆ Full Table 4 is only available at the CDS via anonymous ftp to cdsarc.cds.unistra.fr (130.79.128.5) or via https://cdsarc.cds.unistra.fr/viz-bin/cat/J/A+A/676/A90

⋆⋆ Based on observations made with the Italian Telescopio Nazionale *Galileo* (TNG) operated by the Fundación Galileo Galilei (FGG) of the Istituto Nazionale di Astrofisica (INAF) at the Observatorio del Roque de los Muchachos (La Palma, Canary Islands, Spain).

$R = 115\,000$), and the micro- ($v_{\rm micro}$) and macro- ($v_{\rm macro}$) turbulence broadening. Slowly rotating solar-like and M-type stars are also among the main targets in the exoplanet field; therefore, it is particularly important to have a reliable method to estimate the $v_{\rm eq} \sin i_\star$ for these objects in order to better characterize the host stars. Using the FWHM given by the HARPS-N DRS allows everyone to recover the $v_{\rm eq} \sin i_\star$ values directly for the HARPS-N archival data.

Once it is obtained, the $v_{\rm eq} \sin i_\star$ value may be used along with estimates of the stellar rotational period $P_{\rm rot}$ (for example from photometric time series or spectroscopic time series of activity indices) and the stellar radius $R_\star$ – derived for example from spectral energy distribution (SED) fitting (see Sect. 2) – to recover the stellar inclination $i_\star$:

$$i_\star = \arcsin\left(\frac{P_{\rm rot} \times v_{\rm eq} \sin i_\star}{2\pi R_\star}\right). \quad (1)$$

The stellar inclination heavily affects exoplanets' parameters (Hirano et al. 2014). Having an estimate of its value is also a fundamental step in computing the spin-orbit angle of exoplanetary systems, which is an important observational probe of the origin and evolution of the systems (e.g. Queloz et al. 2000; Winn et al. 2005).

The approach of exploiting known stellar radii and rotational periods to infer the rotational velocity and to calibrate the width of the CCF versus $v_{\rm eq} \sin i_\star$ is not completely new, as it was previously adopted by Nordström et al. (2004). However, in their case, the stellar inclination remained unknown and the additional uncertainty was treated statistically. Instead, in our work we took advantage of the known viewing geometry of stars that host a transiting planet with an orbit inclination close to 90 deg, and a good spin-orbit alignment as inferred by the measurement of the Rossiter-McLaughlin effect (Rossiter 1924; McLaughlin 1924). This allowed us to rely on a sample of objects for which the projected rotational velocity, linked to the CCF width, is similar to the equatorial velocity inferred from the rotational period and the stellar radius. Furthermore, the selection of a sample of transiting planets ensures the availability of high-quality photometric data (which were taken for the planet search itself) and in most cases of additional relevant literature studies from follow-up observations.

This paper is organized as follows: in Sect. 2 we describe the selection procedure for our calibrators. For Sect. 3, we used them to create our empirical relation, and then we applied that to a large set of exoplanet host stars in Sect. 4. We test the applicability of our relation to other spectrographs in Sect. 5, and finally we present our conclusions in Sect. 6.

2. Calibrators' selection and characterization

To calibrate our empirical relation as accurately as possible, we relied on a very strict selection of calibrators. We queried the NASA exoplanet archive[1] to obtain a list of all known exoplanet host stars with *a)* a declination >−25 deg (to ensure they were observable with the TNG), and *b)* an absolute value of the system sky-projected obliquity λ smaller than 30 deg, as derived from the Rossiter-McLaughlin effect and reported in the TEPCat catalogue (Southworth 2011). The latter value is a compromise between the need to have systems that can be considered aligned in such a way that the stellar projected rotational velocity $v_{\rm eq} \sin i_\star$ can be considered approximately equal to the stellar equatorial velocity $v_{\rm eq}$, and the need to have a good number of useful calibrators (at least some tens of objects).

This selection resulted in a list of 66 targets. We then searched the TNG archive for public HARPS-N spectra of these stars, to combine them with the proprietary data obtained within the Global Architecture of Planetary Systems (GAPS) program, which is an Italian project dedicated to the search and characterization of exoplanets (PI G. Micela; Covino et al. 2013). We thus found 44 stars with useful HARPS-N CCFs.

The stellar masks available in the DRS library are optimized for main sequence stars with stellar types G2, K5, and M2. With the new upgrades to the DRS, more masks are starting to be available for different spectral types, and they will have to be calibrated accordingly. However, in this work, we focus on the original masks that have been used so far, and that are still available in the DRS. Unfortunately, the M2 CCFs are useless for our purposes because the use of the M2 mask results in deformed CCF profiles with large bumps in the wings. In a previous work (Rainer et al. 2020), we created an improved M-type mask to overcome this problem, but we do not consider this mask here because it is not publicly available: our scope is to enable astronomers to use the public HARPS-N archival data. Thus, we focus on the G2 and K5 CCFs: while this optimized our work for solar-like stars, some M-type stars may still be reduced using the K5 mask in order to recover the $v_{\rm eq} \sin i_\star$ estimate from the CCF FWHM.

Our selection criteria ensure that $\sin i_\star \approx 1$, which means that we can consider $v_{\rm eq} \sin i_\star \approx v_{\rm eq}$ for all our calibrators. If we are able to estimate the equatorial velocity $v_{\rm eq}$, then we can build a relation between FWHM and $v_{\rm eq} \sin i_\star$ in a straightforward way. In order to compute $v_{\rm eq}$, we needed estimates of the rotational periods $P_{\rm rot}$ and the radii $R_\star$ of our calibrators:

$$v_{\rm eq} = \frac{2\pi \times R_\star}{P_{\rm rot}}. \quad (2)$$

We derived the rotation period $P_{\rm rot}$ mainly from the photometry of the Transiting Exoplanet Survey Satellite (TESS) space mission (Ricker et al. 2015) and the ground-based Super Wide Angle Search for Planets (SuperWASP) project (Butters et al. 2010). In the case of TESS, we used the Pre-search Data Conditioned Simple Aperture Photometry (PDCSAP) light curves (Stumpe et al. 2012) as downloaded from the Mikulski Archive for Space Telescopes[2] (MAST), where systematic artefacts are likely removed by the PDCSAP pipeline. PDCSAP light curves were analysed using the generalized Lomb-Scargle (GLS) periodogram (Zechmeister & Kürster 2009) and the detected periods are listed in Table 1. In the case of the SuperWASP photometric time series, we first disregarded possible outliers, that is data points that deviated more than three standard deviations from the mean of the whole data series. Then, we computed a filtered version of the light curve by means of a sliding median boxcar filter with a boxcar extension equal to 2 h. This filtered light curve was then subtracted from the original light curve, and all the points deviating more than three standard deviations from the residuals were discarded. Finally, we computed normal points by binning the data on time intervals having the duration of about 2 h. The rotation period search was performed by using the GLS and the CLEAN (Roberts et al. 1987) periodogram analysis. All the periodicities detected by GLS, with a false alarm probability smaller than 0.1% (see Horne & Baliunas 1986), and recovered with the same value within the uncertainty, also by CLEAN,

[1] https://exoplanetarchive.ipac.caltech.edu/

[2] https://mast.stsci.edu/portal/Mashup/Clients/Mast/Portal.html

Table 1. Calibrators.

Name	λ [deg]	$T_{\rm eff}$ [K]	$\log g$ [dex]	[Fe/H] [dex]	$P_{\rm rot}$ [days]	$R_\star$ [$R_\odot$]	$v_{\rm micro}$ [km s^{-1}]	$v_{\rm macro}$ [km s^{-1}]
HAT-P-1	3.7	5980 ± 49 [4]	4.36 ± 0.01 [4]	0.13 ± 0.008 [4]	48 ± 5 [1]	1.273 ± 0.065 [3]	1.19 [3]	3.92 [3]
HAT-P-2	9.0	6380 ± 0 [5]	4.16 ± 0.02 [6]	0.13 ± 0.008 [7]	97 ± 10 [1] 2.82 ± 0.05 [2] 96 ± 15 [3]	1.684 ± 0.029 [3]	1.68 [3]	5.90 [3]
HAT-P-3	21.2	5185 ± 80 [6]	4.56 ± 0.03 [6]	0.24 ± 0.08 [8]	28 ± 2 [1] 40 ± 2 [1]	0.861 ± 0.015 [3]	0.59 [3]	2.02 [3]
HAT-P-8	–17.0	6200 ± 80 [6]	4.15 ± 0.03 [6]	0.01 ± 0.08 [7]	4.25 ± 0.05 [1]	1.546 ± 0.027 [3]	1.48 [3]	5.13 [3]
HAT-P-13	1.9	5653 ± 90 [7]	4.13 ± 0.04 [9]	0.41 ± 0.08 [7]	30 ± 3 [1]	1.824 ± 0.038 [3]	0.99 [3]	3.57 [3]
HAT-P-16	–2.0	6158 ± 80 [10]	4.34 ± 0.03 [10]	0.17 ± 0.08 [10]	12.7 ± 0.5 [1]	1.221 ± 0.019 [3]	1.37 [3]	4.58 [3]
HAT-P-17	19.0	5246 ± 80 [6]	4.53 ± 0.02 [6]	0.0 ± 0.08 [7]	33 ± 5 [1] 25 ± 8.3 [2]	0.87 ± 0.018 [3]	0.62 [3]	2.35 [3]
HAT-P-20	–8.0	4595 ± 80 [11]	4.63 ± 0.02 [11]	0.22 ± 0.09 [12]	14.48 ± 0.02 [12] 14.44 ± 0.07 [1]	0.722 ± 0.011 [3]	0.45 [3]	1.53 [3]
HAT-P-22	–2.1	5302 ± 80 [6]	4.36 ± 0.04 [6]	0.30 ± 0.09 [8]	28.7 ± 0.04 [8] 37 ± 1 [1]	1.075 ± 0.024 [3]	0.70 [3]	2.71 [3]
HD 17156	10.0	6040 ± 24 [6]	4.20 ± 0.06 [6]	0.24 ± 0.03 [13]	12.8 ± 0.0 [13]	1.52 ± 0.033 [3]	1.30 [3]	4.44 [3]
HD 63433	8.0	5640 ± 74 [14]	4.53 ± 0.09 [14]	0.017 ± 0.017 [15]	6.45 ± 0.05 [14] 6.25 ± 0.93 [2]	0.911 ± 0.021 [3]	0.85 [3]	2.74 [3]
HD 189733	–0.31	5052 ± 16 [6]	4.49 ± 0.05 [6]	0.03 ± 0.08 [7]	11.95 ± 0.01 [7]	0.787 ± 0.036 [3]	0.56 [3]	1.86 [3]
HD 209458	1.58	6091 ± 10 [6]	4.45 ± 0.02 [6]	0.0 ± 0.05 [7]	10.65 ± 0.75 [7]	1.178 ± 0.028 [3]	1.27 [3]	4.11 [3]
K2-29	1.5	5358 ± 38 [16]	4.54 ± 0.01 [16]	0.03 ± 0.05 [16]	10.79 ± 0.02 [16] 10.41 ± 0.07 [1]	0.847 ± 0.019 [3]	0.67 [3]	2.38 [3]
K2-34	–1.0	6071 ± 90 [17]	4.18 ± 0.02 [17]	–	7.9 ± 0.2 [1]	1.43 ± 0.023 [3]	1.33 [3]	4.58 [3]
Kepler-25	9.4	6354 ± 27 [18]	4.29 ± 0.01 [18]	0.11 ± 0.03 [18]	23.147 ± 0.039 [19]	1.737 ± 0.1 [3]	1.61 [3]	5.52 [3]
Qatar-1	–8.4	5013 ± 93 [20]	4.55 ± 0.01 [20]	0.2 ± 0.1 [7]	23.7 ± 0.1 [20]	0.792 ± 0.013 [3]	0.53 [3]	1.82 [3]
Qatar-2	15.0	4645 ± 50 [21]	4.53 ± 0.01 [21]	0.02 ± 0.08 [21]	18.0 ± 0.2 [22]	0.721 ± 0.012 [3]	0.48 [3]	1.56 [3]
TrES-4	6.3	6200 ± 75 [6]	4.06 ± 0.02 [6]	0.28 ± 0.09 [7]	26.2 ± 2 [1]	1.984 ± 0.028 [3]	1.51 [3]	5.31 [3]
WASP-11	7.0	4800 ± 100 [6]	4.45 ± 0.02 [6]	0.12 ± 0.09 [7]	15.26 ± 0.07 [1]	0.857 ± 0.018 [3]	0.52 [3]	1.64 [3]
WASP-13	8.0	5950 ± 70 [6]	4.06 ± 0.01 [6]	0.0 ± 0.2 [7]	9.66 ± 0.9 [1]	1.581 ± 0.024 [3]	1.25 [3]	4.43 [3]
WASP-14	–14.0	6475 ± 100 [6]	4.07 ± 0.02 [6]	0.0 ± 0.2 [7]	22 ± 3 [1]	0.983 ± 0.037 [3]	1.83 [3]	6.55 [3]
WASP-32	–2.0	6140 ± 95 [6]	4.40 ± 0.02 [6]	0.13 ± 0.1 [7]	11.6 ± 1.0 [7]	1.01 ± 0.077 [3]	1.33 [3]	4.39 [3]
WASP-43	3.5	4400 ± 200 [23]	4.49 ± 0.13 [6]	0.05 ± 0.17 [7]	15.6 ± 0.4 [7] 13.3 ± 5.1 [2]	0.679 ± 0.014 [3]	0.50 [3]	1.46 [3]
WASP-69	0.4	4700 ± 50 [6]	4.50 ± 0.15 [6]	0.15 ± 0.08 [7]	23.07 ± 0.16 [7]	0.836 ± 0.014 [3]	0.49 [3]	1.58 [3]
WASP-84	–0.3	5314 ± 88 [24]	4.40 ± 0.13 [24]	0.0 ± 0.1 [7]	14.36 ± 0.35 [7]	0.822 ± 0.011 [3]	0.69 [3]	2.63 [3]
XO-2N	7.0	5340 ± 50 [25]	4.43 ± 0.01 [26]	0.43 ± 0.05 [7]	28.6 ± 1.3 [7] 35 ± 3 [1]	0.998 ± 0.014 [3]	0.70 [3]	2.59 [3]

Notes. HAT-P-2 is present here, but not used as a calibrator because of its large FWHM value (>20 km s^{-1}).

References. [(1)]SuperWASP; [(2)]TESS; [(3)]this work; [(4)]Nikolov et al. (2014); [(5)]Ment et al. (2018); [(6)]Stassun et al. (2017); [(7)]Bonomo et al. (2017); [(8)]Mancini et al. (2018); [(9)]Sada & Ramón-Fox (2016); [(10)]Buchhave et al. (2010); [(11)]Bakos et al. (2011); [(12)]Esposito et al. (2017); [(13)]Fischer et al. (2007); [(14)]Mann et al. (2020); [(15)]`https://exofop.ipac.caltech.edu`; [(16)]Santerne et al. (2016); [(17)]Livingston et al. (2018); [(18)]Benomar et al. (2014); [(19)]McQuillan et al. (2013); [(20)]Collins et al. (2017); [(21)]Močnik et al. (2017); [(22)]Mancini et al. (2014); [(23)]Hellier et al. (2011); [(24)]Anderson et al. (2014); [(25)]Southworth (2012); [(26)]Crouzet et al. (2012).

were considered as the star's rotation period and listed in Table 1. To compute the error associated with the period, we followed the method used by Lamm et al. (2004).

We also checked the spectroscopic activity indicators' time series: we investigated the $R'_{\rm HK}$ activity index using GLS. In general, we did not find any conclusive results given that for most stars only a small number of observations sparsely obtained over a few years were available. In a few cases, the periodogram analysis provided $P_{\rm rot}$ detection, which was always consistent with the photometrically determined period. For the sake of sample homogeneity, we thus considered only the photometric periods.

The stellar radii $R_\star$ were obtained by fitting the SED via the MESA Isochrones and Stellar Tracks (MIST, Dotter 2016; Choi et al. 2016) through the `EXOFASTv2` suite (Eastman et al. 2019). Specifically, we fitted the available archival magnitudes of each star in the sample imposing Gaussian priors on the effective temperature $T_{\rm eff}$ and metallicity [Fe/H] based on the respective literature values listed in Table 1 and on the parallax π based on the *Gaia* EDR3 astrometric measurement (Gaia Collaboration 2016, 2021). Since the SED primarily constrains $R_\star$ and $T_{\rm eff}$, the stellar parameters are simultaneously constrained by the SED and the MIST isochrones, and a penalty for straying from

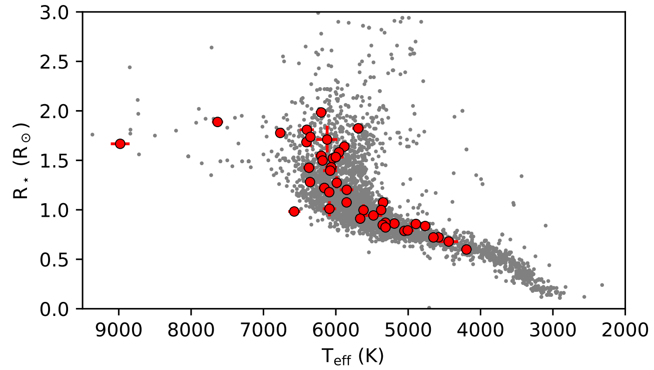

Fig. 1. Comparison in the $T_{\rm eff}$-$R_\star$ parameter space between the sample of stars analysed in this work (red circles) and the currently known exoplanet-host stars (grey dots) as retrieved from the NASA Exoplanet Catalog.

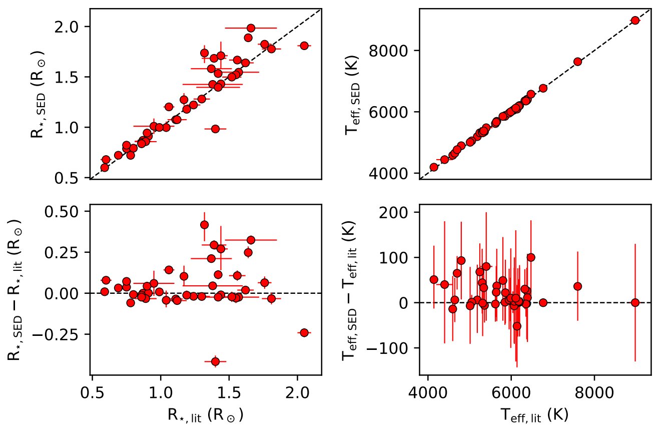

Fig. 2. Comparison of the stellar radii and effective temperatures obtained via the SED fitting described in Sect. 2 with literature values. Upper panels: correlations' plot between our values and the literature ones for $R_\star$ (left panel) and $T_{\rm eff}$ (right panel). Lower panels: residual plots showing the difference between our values and the literature ones.

the MIST evolutionary tracks ensures that the resulting star realization is physical in nature (see Eastman et al. 2019, for more details on the method). In Fig. 1 we show our results compared with the $R_\star$ and $T_{\rm eff}$ of the exoplanet-host stars present in the NASA archive, while in Fig. 2 we show the correlation and residuals between our values and those from the literature.

We also checked the literature for asteroseismic and interferometric radii, which we found for HD 17156 (asteroseismic $R_\star = 1.5007 \pm 0.0076\,R_\odot$, Nutzman et al. 2010), as well as HD 189733 and HD 209458 (interferometric $R_\star$ 0.805 ± 0.016 and $1.203 \pm 0.06\,R_\odot$, respectively, Boyajian et al. 2014). We note that they are in good agreement with our results.

Thus we obtained our semi-final calibrators' list, which is shown in Table 1: 27 stars with known $P_{\rm rot}$ and $R_\star$. In the end, all our calibrators have $\lambda < 21.2$ degrees, strengthening our assumption of $v_{\rm eq} \approx v_{\rm eq} \sin i_\star$.

We also checked the *Gaia* DR3 archive to ensure that we are working with single stars: K2-29 has a fainter companion separated by ≈4.4 arcsec with $\Delta V = 1.8$, and TrES-4 has a fainter companion separated by ≈1.6 arcsec with $\Delta V = 4.9$. We considered that in both cases the combination of the faintness and the distance of the companions allowed us to keep the stars in our calibrators' list.

Using the stellar parameters $T_{\rm eff}$ and $\log g$ from the literature, we estimated the micro- ($v_{\rm micro}$) and macro- ($v_{\rm macro}$) turbulence velocities for each object. In particular, $v_{\rm micro}$ was obtained with Adibekyan et al. (2012) relationships that are valid for stars with $4500 < T_{\rm eff} < 6500$ K, $3.0 < \log g < 5.0$, and $-1.4 <$ [Fe/H] $<$ 0.5 dex. Regarding $v_{\rm macro}$, it was computed with the calibration obtained by Doyle et al. (2014) using asteroseismic rotational velocities for the stars with $T_{\rm eff} > 5700$ K, while for the stars with $T_{\rm eff} < 5700$ K we used the empirical relationship by Brewer et al. (2016). Both relations are valid for dwarf stars (see also Biazzo et al. 2022). To estimate the errors on our $v_{\rm micro}$ and $v_{\rm macro}$, we considered the root-mean-square (rms) error given in the papers, which is larger than the errors derived from the parameters. The rms values are 0.18 km s^{-1} for $v_{\rm micro}$, 0.73 km s^{-1} for $v_{\rm macro}$ from Doyle et al. (2014) ($T_{\rm eff} > 5700$ K), and 0.5 km s^{-1} for $v_{\rm macro}$ from Brewer et al. (2016) ($T_{\rm eff} < 5700$ K).

We note that HAT-P-2 has $P_{\rm rot} = 2.82 \pm 0.05$ days from TESS photometry, but a completely different value from SuperWASP (97 ± 10 days). Applying Eq. (2), the TESS value yields $v_{\rm eq} = 30.12$ km s^{-1}, and the SuperWASP value $v_{\rm eq} = 0.88$ km s^{-1}. The TESS value is nearer to the $v_{\rm eq} \sin i_\star = 20.12 \pm 0.9$ km s^{-1} result obtained from the Fourier transform of the CCF and with the 20.8 ± 0.03 km s^{-1} value from the literature (Bonomo et al. 2017), but there is still a large discrepancy. In any case, this fast rotation excludes this star from being a useful calibrator (see Sect. 3): the final calibrators' list thus contains the stars in Table 1 with the exception of HAT-P-2.

3. Creating the empirical relation

In order to create our empirical relation, we used as inputs the FWHM of the CCFs of the HARPS-N spectra (as computed by the HARPS-N DRS and stored in the keyword `HIERARCH TNG DRS CCF FWHM` of the CCF FITS files), the stellar radii $R_\star$ from Table 1, the rotational periods $P_{\rm rot}$ from Table 1, and the $v_{\rm micro}$ and $v_{\rm macro}$ values from Table 1.

Using the archival CCFs, we are limited by the standard CCF half window of the HARPS-N DRS (20 km s^{-1}): while it may be manually changed, the majority of the archival data have this value. We also note that a more precise $v_{\rm eq} \sin i_\star$ could be recovered for faster rotating stars using rotational fitting or the Fourier transform method, instead of any empirical relation. We thus limited the applicability range of our relation to FWHM up to 20 km s^{-1}, which is a slightly larger value than the maximum FWHM that can be reliably computed with a half window of 20 km s^{-1}, that is ≈16–18 km s^{-1}.

To check this applicability range, we built a range of synthetic CCF profiles by convolving a Gaussian function with the same FWHM of the HARPS-N resolution (≈2.6 km s^{-1}) with different rotational profiles ($v_{\rm eq} \sin i_\star$ ranging from 0.2 to 50 km s^{-1} with a step of 0.2 km s^{-1}). The rotational profiles were built using the following equation from Gray (2008):

$$f(x) = 1 - a\frac{2(1-u)\sqrt{1-\left(\frac{x-x_0}{x_l}\right)^2} + 0.5\pi u\left[1-\left(\frac{x-x_0}{x_l}\right)^2\right]}{\pi x_l\left(1-\frac{u}{3}\right)}, \qquad (3)$$

where a is the depth of the profile, x_0 the centre (i.e. the radial-velocity value), x_l the $v_{\rm eq} \sin i_\star$ of the star, and u the linear limb darkening (LD) coefficient, which we kept fixed as $u = 0.6$.

We fitted the resulting profiles with a Gaussian (see Fig. 3) and compared the Gaussian FWHM with the input $v_{\rm eq} \sin i_\star$ to check their correlation. We chose a Gaussian fit to be consistent

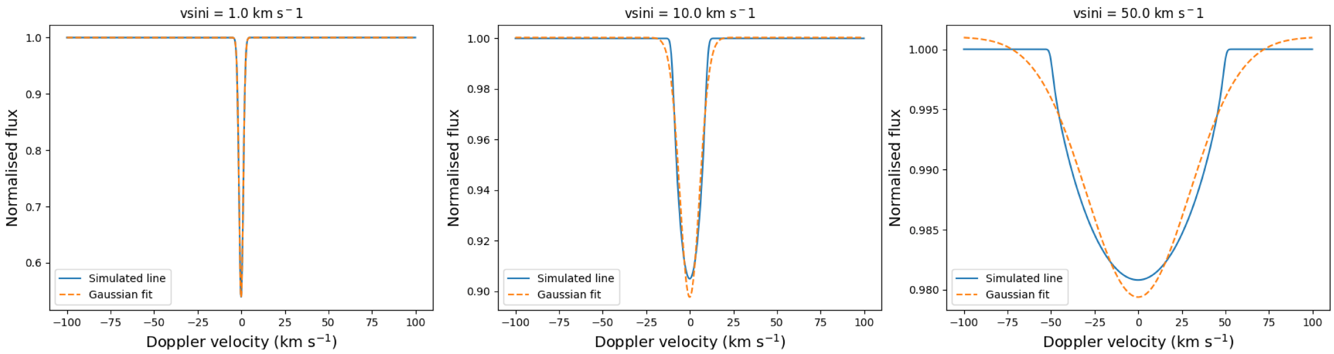

Fig. 3. Simulated CCF (solid blue line) and Gaussian fitting (dashed orange line). Left: input value $v_{\rm eq} \sin i_\star$ = 1 km s^{-1}. Center: input value $v_{\rm eq} \sin i_\star$ = 10 km s^{-1}. Right: input value $v_{\rm eq} \sin i_\star$ = 50 km s^{-1}.

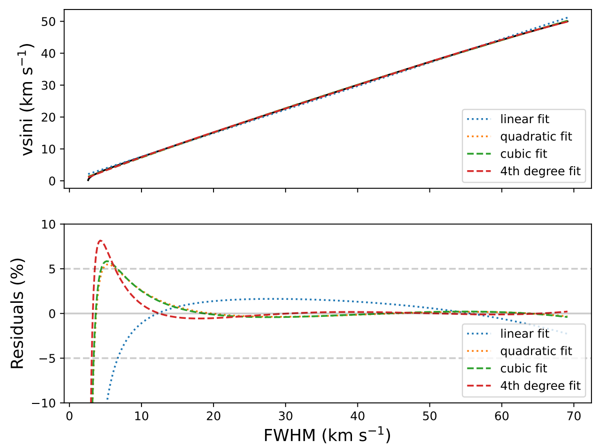

Fig. 4. Correlation between the Gaussian fit's FWHM and the input $v_{\rm eq} \sin i_\star$ of the synthetic line profiles in the whole 0–50 km s^{-1} $v_{\rm eq} \sin i_\star$ (0–70 km s^{-1} FWHM) range. Upper panel: correlation between the FWHM and $v_{\rm eq}$ (black line) and the relative linear fit (blue dotted line), quadratic fit (orange dotted line), cubic fit (green dashed line), and fourth degree polynomial fit (red dashed line). Lower panel: residuals of the fits. The horizontal grey lines outline the 5% difference between the fit and the data.

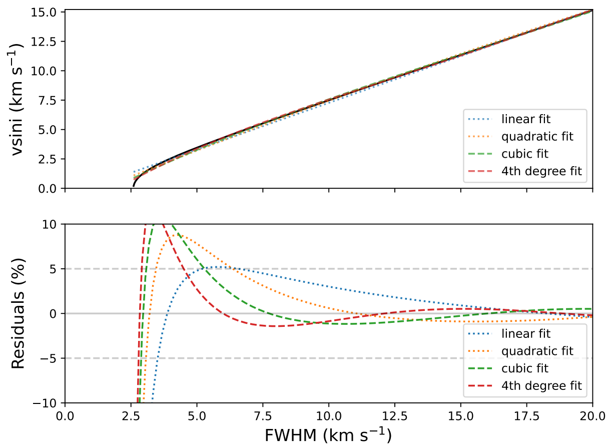

Fig. 5. Same as Fig. 4, but limited to the 0–20 km s^{-1} FWHM range.

with HARPS-N DRS, which recovers both the radial velocity and the FWHM with a Gaussian fit of the CCF.

Using a single fit for the whole range resulted in some discrepancy at the borders, in particular for low FWHM values ($FWHM < 6.5$ km s^{-1}), that is the range we are more interested in (see Fig. 4). As such we decided to try and improve the fit at lower values and limit our FWHM fitting range to 0–20 km s^{-1}: in this case, while higher-order polynomials behave well enough down to $FWHM = 5$ km s^{-1}, the linear fit residuals lie below 5% down to $FWHM = 3.5$ km s^{-1} (see Fig. 5). Considering that we have a small sample of calibrators (which hinders our ability to constrain a high degree polynomial), and that the linear fit recovers the $v_{\rm eq} \sin i_\star$ values with a 5% error at worst, we can then reasonably assume that using a linear fit on the calibrators with $FWHM < 20$ km s^{-1} would give us useful results. Taking all of the previous considerations into account, such as the default half-window value of the CCFs, the aim to optimize the FWHM-$v_{\rm eq} \sin i_\star$ relation for the lower FWHM values, and above all the small sample of calibrators of which only one object (HAT-P-2) has $FWHM > 20$km s^{-1}, we then excluded HAT-P-2 from the final calibrators' list and consider our work reliably applicable only for $FWHM < 20$ km s^{-1}.

The simple test done with our simulated CCFs does not take all of the other non-constant causes of broadening into account: for example, the effects of $v_{\rm micro}$ and $v_{\rm macro}$, which highly depend on the stellar type, are not considered. A more detailed test would involve studying the CCFs obtained on a range of synthetic spectra with different $v_{\rm eq} \sin i_\star$ and stellar parameters; unfortunately, the HARPS-N DRS works only on real raw HARPS-N data, so we cannot perform this analysis. However, we were still able to test our final results in this sense, because while our calibrators' sample is quite small, the total number of stars for which we computed $v_{\rm eq} \sin i_\star$, and that have literature values of $v_{\rm eq} \sin i_\star$ to compare them to, is large enough to allow us to look for trends or misbehaviour related to the stellar parameters (see Sect. 4).

We created our relation first by using the CCFs computed with the G2 mask, and then we repeated the work described hereafter also for the K5 CCFs. We built four data sets: (a) the original FWHM computed by the DRS (FWHM$_{\rm DRS}$); (b) the FWHM$_{\rm DRS}$ minus the $v_{\rm micro}$ broadening (FWHM$_{\rm mic}$); (c) the FWHM$_{\rm DRS}$ minus the $v_{\rm macro}$ broadening (FWHM$_{\rm mac}$); (d) and the FWHM$_{\rm DRS}$ minus both $v_{\rm micro}$ and $v_{\rm macro}$ broadening (FWHM$_{\rm mic+mac}$). We also considered removing the instrumental broadening, but since this is a constant effect in HARPS-N spectra it is simply included in the empirical relation. The values of FWHM$_{\rm mic}$, FWHM$_{\rm mac}$, and FWHM$_{\rm mic+mac}$ are obtained with the following equations:

$$FWHM_{\rm mic} = \sqrt{FWHM_{\rm DRS}{}^2 - v_m^2} \quad (4)$$

$$FWHM_{\rm mac} = \sqrt{FWHM_{\rm DRS}{}^2 - v_M^2} \quad (5)$$

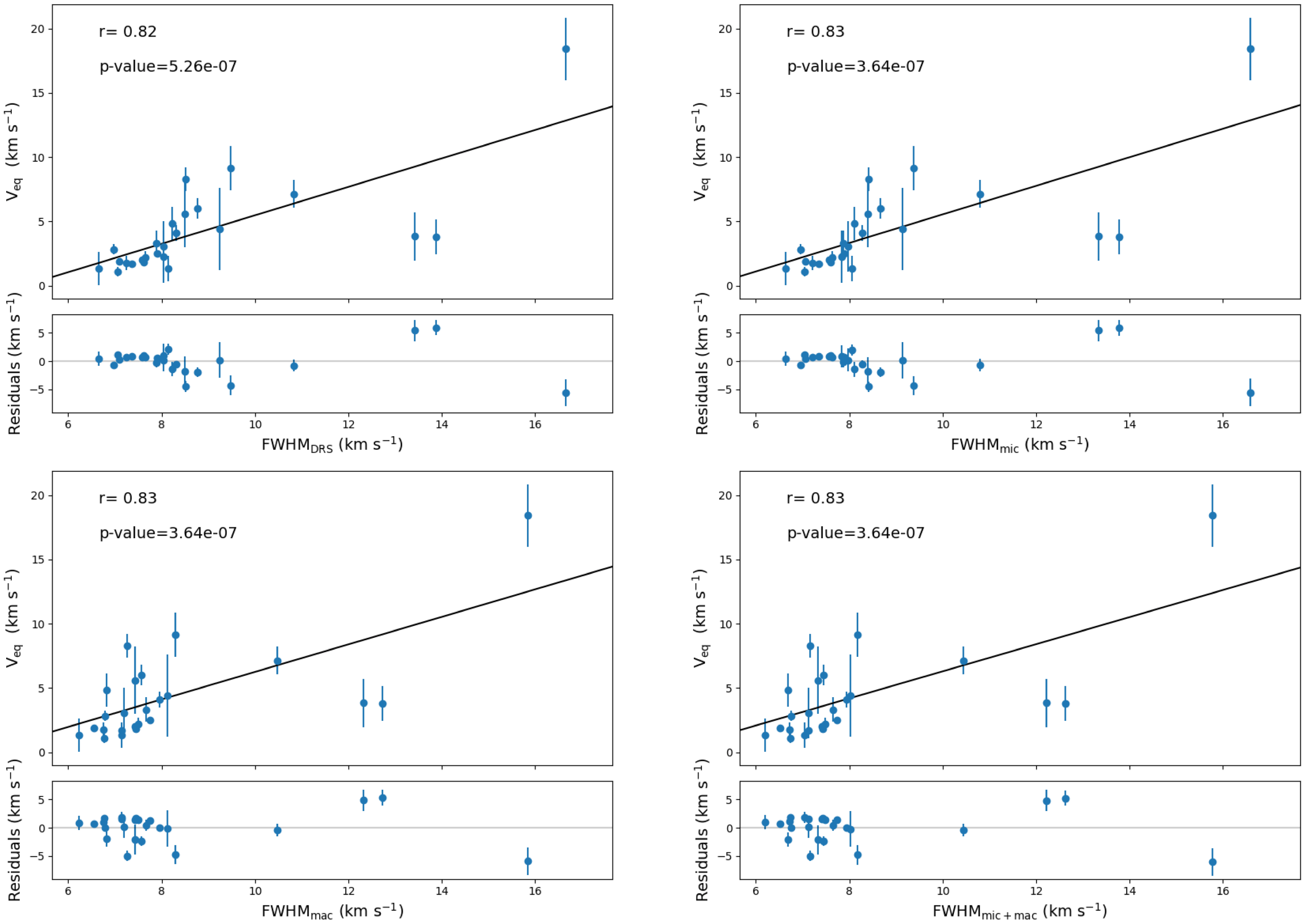

Fig. 6. Linear correlations (black solid lines) between the four data sets derived from the FWHM$_{\rm DRS}$ computed by the HARPS-N DRS with the G2 mask (x-axis) and the stellar equatorial velocity $v_{\rm eq}$ (y-axis) for our set of calibrators. The Spearman's correlation coefficient r and p-value are shown in the plots. Upper left: linear correlation between FWHM$_{\rm DRS}$ and $v_{\rm eq}$ and relative residuals. Upper right: linear correlation between FWHM$_{\rm mic}$ and $v_{\rm eq}$ and relative residuals. Lower left: linear correlation between FWHM$_{\rm mac}$ and $v_{\rm eq}$ and relative residuals. Lower right: linear correlation between FWHM$_{\rm mic+mac}$ and $v_{\rm eq}$ and relative residuals.

$$FWHM_{\rm mic+mac} = \sqrt{FWHM_{\rm DRS}{}^2 - v_m^2 - v_M^2}. \tag{6}$$

We fitted a linear relation to each one of our four data sets (Fig. 6): (a) FWHM$_{\rm DRS}$ versus $v_{\rm eq}$, (b) FWHM$_{\rm mic}$ versus $v_{\rm eq}$, (c) FWHM$_{\rm mac}$ versus $v_{\rm eq}$, and (d) FWHM$_{\rm mic+mac}$ versus $v_{\rm eq}$. The three leftmost points (TrES-4, Kepler-25, and HAT-P-8 from lower to higher FWHM, respectively) may appear as outliers, but we decided to keep them for several reasons: there are very few calibrators with $FWHM > 10$ km s^{-1}, we have no solid reason to mistrust the $P_{\rm rot}$ and $R_\star$ values used in our work, and the $v_{\rm eq} \sin i_\star$ computed with the resulting calibrations for hundreds of exoplanet-host stars agree well with the literature values (see Sect. 4).

As final relation, we used the most simple and straightforward one, which links the FWHM$_{\rm DRS}$ as it is and the $v_{\rm eq} \sin i_\star$ linearly (Fig. 6, upper left panel), as this is the relation that may be more widely useful because it does not depend on knowledge of $v_{\rm micro}$ and $v_{\rm macro}$. The resulting calibrations using the G2 and K5 masks are thus

$$\begin{aligned} \text{G2 mask} : v_{\rm eq} \sin i_\star &= 1.09446 \times FWHM_{\rm DRS} - 5.45380 \\ \text{K5 mask} : v_{\rm eq} \sin i_\star &= 1.26952 \times FWHM_{\rm DRS} - 6.06771\text{'} \end{aligned} \tag{7}$$

respectively.

For completeness' sake, here, we also provide the calibrations obtained for FWHM$_{\rm mic}$ (Eq. (8)), FWHM$_{\rm mac}$ (Eq. (9)), and FWHM$_{\rm mic+mac}$ (Eq. (10)):

$$\begin{aligned} \text{G2 mask} : v_{\rm eq} \sin i_\star &= 1.09886 \times FWHM_{\rm mic} - 5.42695 \\ \text{K5 mask} : v_{\rm eq} \sin i_\star &= 1.27563 \times FWHM_{\rm mic} - 6.04075 \end{aligned} \tag{8}$$

$$\begin{aligned} \text{G2 mask} : v_{\rm eq} \sin i_\star &= 1.05962 \times FWHM_{\rm mac} - 4.33315 \\ \text{K5 mask} : v_{\rm eq} \sin i_\star &= 1.23413 \times FWHM_{\rm mac} - 4.81863 \end{aligned} \tag{9}$$

$$\begin{aligned} \text{G2 mask} : v_{\rm eq} \sin i_\star &= 1.0438 \times FWHM_{\rm mic+mac} - 4.13 \\ \text{K5 mask} : v_{\rm eq} \sin i_\star &= 1.21346 \times FWHM_{\rm mic+mac} - 4.57564. \end{aligned} \tag{10}$$

To estimate the errors on our $v_{\rm eq} \sin i_\star$ measurements, we applied error propagation theory. Considering that all our equations are linear fits structured as $v_{\rm eq} \sin i_\star = aFWHM + b$, we could derive the error on $v_{\rm eq} \sin i_\star$ using the following equation:

$$\sigma_{v_{\rm eq} \sin i_\star} = \sqrt{FWHM^2 \sigma_a{}^2 + \sigma_b{}^2 + 2FWHM \sigma_a \sigma_b \rho(a,b)}, \tag{11}$$

Table 2. Fit parameters a and b, uncertainties σ_a and σ_b, and correlation factor $\rho(a,b)$ for all the relevant equations obtained in this paper.

Equation	Mask	a	b	σ_a	σ_b	$\rho(a,b)$
(7)	G2	1.09446	−5.45380	0.21854	2.00007	−0.96604
(7)	K5	1.26952	−6.06771	0.19402	1.62830	−0.96250
(8)	G2	1.09886	−5.42695	0.21989	1.9991	−0.96592
(8)	K5	1.27563	−6.04075	0.19522	1.62635	−0.96238
(9)	G2	1.05962	−4.33315	0.23369	1.96348	−0.96100
(9)	K5	1.23413	−4.81863	0.21586	1.64721	−0.95615
(10)	G2	1.0438	−4.13	0.23468	1.95621	−0.95998
(10)	K5	1.21346	−4.57564	0.21850	1.65255	−0.95471
(14)	G2	1.1241	−5.70685	0.03629	0.32201	−0.9657
(15)	K5	1.34470	−6.69438	0.08660	0.57299	−0.99065

where σ_a and σ_b are the uncertainties in the fit parameters, while $\rho(a,b)$ is the correlation coefficient,

$$\rho(a,b) = \frac{-\sum_{i=1}^{N} FWHM_i}{\sqrt{N\sum_{i=1}^{N} FWHM_i^2}}. \tag{12}$$

The values of σ_a, σ_b, and $\rho(a,b)$ for all the Eqs. (7)–(10) are listed in Table 2. We have no estimate for the error of $\mathrm{FWHM_{DRS}}$ because unfortunately this information is not stored in the header of the FITS files, but we tried to recover it by checking the standard deviation of the $\mathrm{FWHM_{DRS}}$ values when more than one CCF was available. We found a standard deviation of the order of 4%, which is much lower than the other contributions to the error budget. Thus we deemed Eq. (11) sufficient to estimate the errors in $v_{\rm eq}\sin i_\star$ derived from Eq. (7). Concerning Eqs. (8)–(10) instead, the error on $v_{\rm micro}$ and $v_{\rm macro}$ is expected to propagate on the FWHM, resulting in the FWHM errors $\sigma_{\mathrm{FWHM_{mic}}}$, $\sigma_{\mathrm{FWHM_{mac}}}$, and $\sigma_{\mathrm{FWHM_{mic+mac}}}$. The total error whould then be the following:

$$\sigma_{\rm tot} = \sqrt{\sigma^2_{v_{\rm eq}\sin i_\star} + a^2\sigma^2_{\rm FWHM}}. \tag{13}$$

As stated before, we used the rms as errors on $v_{\rm micro}$ and $v_{\rm macro}$, with 0.18 km s^{-1} for $v_{\rm micro}$, either 0.5 or 0.73 km s^{-1} for $v_{\rm macro}$ depending of the star's temperature, the former for $T_{\rm eff} < 5700$ K, and the latter for $T_{\rm eff} > 5700$ K. These values are larger than what we would obtain propagating the errors on the stellar parameters.

We compared the results obtained with the different calibration on our calibrators set (see Table 3), and the $v_{\rm eq}\sin i_\star$ agree to the order of 0.2–0.3 km s^{-1} with the exception of WASP-14, where Eqs. (7) and (8) give very different results from Eqs. (9) and (10): WASP-14 is the hottest star in our calibrators' set, with the largest $v_{\rm micro}$ and $v_{\rm macro}$ values, and the problems may arise from over-estimating these values due to the stellar $T_{\rm eff}$ being at the edge of the applicability range of the relationships used to compute them.

4. Projected rotational velocity of exoplanet-host stars

We decided to apply our relation to all the HARPS-N observed exoplanet-host stars found in the TNG archive. First, we queried the NASA exoplanet archive again to obtain a complete list of all known exoplanet-host stars with a declination > −25 deg, without any other constraints. We obtained a preliminary list of 3750 exoplanets (2753 host stars).

We queried the TNG archive[3] with a self-written `python` code using the `pyvo` module[4] in an asynchronous Table Access Protocol (TAP) query, retrieving up to ten public CCF FITS files for each target. We found data for 313 stars, but some of them are useless for different reasons, for example fast rotating stars, a signal-to-noise ratio (S/N) that is too low, and M-type stars having been reduced with the M2 mask.

We point out here that the CCFs of M-type stars may be used if they are computed with the K5 mask: this results in a noisier, but more physically significant CCF. We were also able to recover the M-type stars reduced with the M2 mask that were observed within the GAPS program: in this case, we could once again reduce the spectra with the K5 mask using the YABI platform (Hunter et al. 2012) hosted at the IA2 Data Center[5].

In the end, we had to discard some non-GAPS stars with only M2-mask public CCFs, and others stars whose CCFs had a S/N that was too low, or the wrong input radial velocity. We estimated the $v_{\rm eq}\sin i_\star$ for all the 273 remaining targets with $FWHM_{\rm DRS} <$ 20 km s^{-1}. The full table with our $v_{\rm eq}\sin i_\star$ values is available at CDS, an extract is shown in Table 4; the errors were computed using Eq. (11).

Some of the objects in our sample have both G2 and K5 CCFs in the TNG archive, and so we were able to directly compare the results of the two calibrations, in order to quantify the effect of a spectral-type mismatch on the resulting $v_{\rm eq}\sin i_\star$ (see Fig. 7). These objects have a relatively small range of $v_{\rm eq}\sin i_\star$, but still the results agree with less than a 0.5 km s^{-1} difference for $v_{\rm eq}\sin i_\star < 4$ km s^{-1}, and with less than 1 km s^{-1} for $v_{\rm eq}\sin i_\star > 4$ km s^{-1}. Still, to ensure the best possible result, care should be taken to reduce every star with the more appropriate mask. Usually this is already done, because the better the star-mask match, the smaller the error is for the radial velocity computed by the DRS, but sometimes the stellar type is unknown prior to the observations and a mismatch may occur. Possible mismatches between hotter stars (early F-type or above) and the G2 mask are not considered here because hotter stars are usually also fast rotators and they would naturally fall outside the applicability range of our relation ($FWHM_{\rm DRS} < 20$ km s^{-1}). Because we relied on the public data present in the TNG archive, there are a few mismatches between the stellar type and mask in our sample, but in all these cases we have $v_{\rm eq}\sin i_\star < 4$ km s^{-1}, so the mismatches should not heavily affect the results.

[3] http://archives.ia2.inaf.it/tng/
[4] https://pyvo.readthedocs.io/en/latest/index.html
[5] https://www.ia2.inaf.it

Table 3. Comparison between $v_{eq} \sin i_\star$ obtained with the different Eqs. (7)–(10) for our calibrators, along with the standard deviation of the results.

Name	$v_{eq} \sin i_\star$ [km s^{-1}]	$v_{eq} \sin i_{\star mic}$ [km s^{-1}]	$v_{eq} \sin i_{\star mac}$ [km s^{-1}]	$v_{eq} \sin i_{\star mic+mac}$ [km s^{-1}]	Std. dev. [km s^{-1}]	Mask used for the CCF	Sp. type
HAT-P-1	3.46 ± 0.54	3.43 ± 0.54	3.23 ± 0.72	3.22 ± 0.73	0.11	G2	G0V
	3.81 ± 0.45	3.76 ± 0.45	3.47 ± 0.72	3.45 ± 0.73	0.16	K5	G0V
HAT-P-3	2.28 ± 0.65	2.31 ± 0.64	2.84 ± 0.64	2.91 ± 0.64	0.29	G2	K1V
	1.88 ± 0.57	1.91 ± 0.59	2.49 ± 0.6	2.58 ± 0.60	0.32	K5	K1V
HAT-P-8	12.77 ± 1.78	12.80 ± 1.79	12.45 ± 1.91	12.33 ± 1.92	0.20	G2	F8V
	15.55 ± 1.65	15.6 ± 1.66	15.22 ± 1.85	15.05 ± 1.87	0.23	K5	F8V
HAT-P-13	3.34 ± 0.55	3.34 ± 0.55	3.30 ± 0.64	3.31 ± 0.64	0.01	G2	G4
HAT-P-16	3.54 ± 0.53	3.48 ± 0.54	2.90 ± 0.81	2.85 ± 0.82	0.32	G2	F8
	3.91 ± 0.44	3.83 ± 0.45	3.06 ± 0.83	2.99 ± 0.84	0.42	K5	F8
HAT-P-17	1.84 ± 0.70	1.86 ± 0.70	2.27 ± 0.72	2.34 ± 0.72	0.23	G2	G0
	1.75 ± 0.58	1.77 ± 0.58	2.20 ± 0.65	2.29 ± 0.65	0.25	K5	G0
HAT-P-20	3.20 ± 0.56	3.24 ± 0.55	3.88 ± 0.56	3.95 ± 0.56	0.35	G2	K3V
	2.92 ± 0.48	2.97 ± 0.48	3.71 ± 0.51	3.79 ± 0.51	0.40	K5	K3V
HAT-P-22	2.31 ± 0.64	2.33 ± 0.64	2.62 ± 0.68	2.68 ± 0.68	0.17	G2	G5
	2.26 ± 0.53	2.28 ± 0.53	2.55 ± 0.63	2.62 ± 0.63	0.16	K5	G5
HD17156	4.14 ± 0.52	4.10 ± 0.52	3.68 ± 0.72	3.64 ± 0.72	0.23	G2	F9V
	4.61 ± 0.45	4.56 ± 0.45	4.00 ± 0.74	3.95 ± 0.75	0.31	K5	F9V
HD63433	6.40 ± 0.67	6.43 ± 0.68	6.77 ± 0.79	6.77 ± 0.80	0.18	G2	G5V
	7.23 ± 0.64	7.28 ± 0.65	7.66 ± 0.79	7.65 ± 0.81	0.20	K5	G5V
HD189733	3.18 ± 0.56	3.22 ± 0.56	3.79 ± 0.57	3.85 ± 0.57	0.31	G2	K2V
	3.11 ± 0.47	3.15 ± 0.47	3.80 ± 0.51	3.87 ± 0.52	0.35	K5	K2V
HD209458	3.84 ± 0.52	3.80 ± 0.53	3.55 ± 0.71	3.52 ± 0.71	0.14	G2	F9V
	4.30 ± 0.44	4.25 ± 0.44	3.89 ± 0.71	3.85 ± 0.72	0.20	K5	F9V
K2-29	3.64 ± 0.53	3.67 ± 0.53	4.10 ± 0.57	4.15 ± 0.57	0.24	G2	K2V
	3.79 ± 0.45	3.82 ± 0.45	4.30 ± 0.52	4.35 ± 0.53	0.26	K5	K2V
K2-34	4.91 ± 0.53	4.88 ± 0.53	4.45 ± 0.69	4.41 ± 0.70	0.23	G2	G2V
	5.59 ± 0.49	5.55 ± 0.49	5.01 ± 0.72	4.95 ± 0.73	0.30	K5	G2V
Kepler-25	9.73 ± 1.21	9.71 ± 1.21	9.15 ± 1.26	9.04 ± 1.26	0.32	G2	–
Qatar-1	2.61 ± 0.61	2.65 ± 0.61	3.23 ± 0.60	3.30 ± 0.60	0.32	G2	–
	2.28 ± 0.53	2.32 ± 0.53	2.98 ± 0.56	3.07 ± 0.56	0.36	K5	–
Qatar-2	2.85 ± 0.58	2.90 ± 0.58	3.54 ± 0.57	3.61 ± 0.58	0.35	G2	K5V
	2.45 ± 0.52	2.50 ± 0.51	3.24 ± 0.53	3.32 ± 0.54	0.40	K5	K5V
TrES-4	9.23 ± 1.12	9.22 ± 1.13	8.72 ± 1.18	8.63 ± 1.18	0.28	G2	–
	10.55 ± 1.05	10.54 ± 1.05	9.94 ± 1.17	9.82 ± 1.17	0.34	K5	–
WASP-11	2.18 ± 0.66	2.22 ± 0.65	2.85 ± 0.63	2.93 ± 0.63	0.35	G2	K3V
	1.84 ± 0.57	1.87 ± 0.57	2.59 ± 0.58	2.69 ± 0.59	0.39	K5	K3V
WASP-13	3.86 ± 0.52	3.82 ± 0.52	3.36 ± 0.74	3.34 ± 0.75	0.25	G2	G1V
	4.30 ± 0.44	4.25 ± 0.44	3.64 ± 0.76	3.60 ± 0.77	0.33	K5	G1V
WASP-14	3.35 ± 0.55	3.18 ± 0.56	0.61 ± 1.45	0.35 ± 1.55	1.40	G2	F5V
	3.75 ± 0.45	3.54 ± 0.46	0.25 ± 1.66	0.00 ± 1.83	1.79	K5	F5V
WASP-32	4.66 ± 0.52	4.62 ± 0.52	4.28 ± 0.68	4.24 ± 0.69	0.19	G2	–
	5.28 ± 0.47	5.23 ± 0.47	4.79 ± 0.71	4.73 ± 0.71	0.25	K5	–
WASP-43	2.91 ± 0.58	2.96 ± 0.58	3.62 ± 0.57	3.68 ± 0.57	0.36	G2	K7V
	2.68 ± 0.50	2.73 ± 0.50	3.50 ± 0.51	3.58 ± 0.52	0.42	K5	K7V
WASP-69	2.87 ± 0.58	2.92 ± 0.58	3.55 ± 0.57	3.62 ± 0.58	0.35	G2	–
	2.51 ± 0.51	2.56 ± 0.51	3.29 ± 0.53	3.38 ± 0.53	0.40	K5	–
WASP-84	2.97 ± 0.48	3.00 ± 0.48	3.35 ± 0.56	3.41 ± 0.57	0.20	K5	–
XO-2N	2.47 ± 0.62	2.49 ± 0.62	2.83 ± 0.66	2.89 ± 0.66	0.19	G2	G9V
	2.27 ± 0.53	2.28 ± 0.53	2.63 ± 0.61	2.69 ± 0.62	0.19	K5	G9V

Notes. The spectral types are taken from SIMBAD.

4.1. Comparison with the literature

Out of the stars listed in Table 4, 206 had also $v_{eq} \sin i_\star$ values from the literature, so we could compare our results with them (see Fig. 8). As a sanity check, we used this larger sample to test our relations: we calibrated the G2 and K5 $\mathrm{FWHM_{DRS}}$ values using the whole set of literature $v_{eq} \sin i_\star$ values. The resulting relations are as follows:

$$\begin{aligned} &\text{G2 mask}: v_{eq} \sin i_\star = 1.1241 \times FWHM_{DRS} - 5.70685 \\ &\text{K5 mask}: v_{eq} \sin i_\star = 0.95935 \times FWHM_{DRS} - 4.37978. \end{aligned} \quad (14)$$

Table 4. Computed $v_{eq} \sin i_\star$ of exoplanet-host stars.

Name	Sp. type	DRS mask	$FWHM_{DRS}$ (km s^{-1})	$v_{eq} \sin i_\star$ (km s^{-1})	Lit. $v_{eq} \sin i_\star$ (km s^{-1})	Reference
2MASS J22362452 +4751425	–	K5	7.44	3.38 ± 0.46	–	–
24 Sex	K0IV	G2	7.26	2.49 ± 0.62	2.77 ± 0.5	Johnson et al. (2011)
51 Peg	G2IV	G2	7.31	2.54 ± 0.62	2.2 ± 1.0	Mayor & Queloz (1995)
55 Cnc	K0IV-V	G2	7.08	2.30 ± 0.64	2.0 ± 0.0	Butler et al. (1997)
BD+03 2562	K2	K5	8.05	4.15 ± 0.44	2.7 ± 0.3	Villaver et al. (2017)
...	...	...	...	...	...	...

Notes. When more than one spectrum is found in the archive, the $FWHM_{DRS}$ is obtained as the mean of a maximum of ten values. The spectral types are taken from SIMBAD. The full table is available at the CDS.

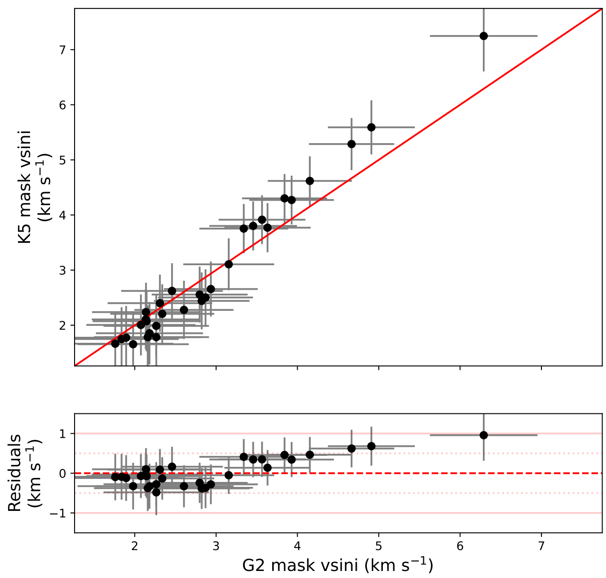

Fig. 7. Results obtained with the G2 and the K5 relations for a subset of stars where both CCFs are available. Upper panel: comparison between $v_{eq} \sin i_\star$ obtained with the G2 relation (x-axis) and the K5 relation (y-axis). The red line shows the one-to-one correlation. Lower panel: residuals.

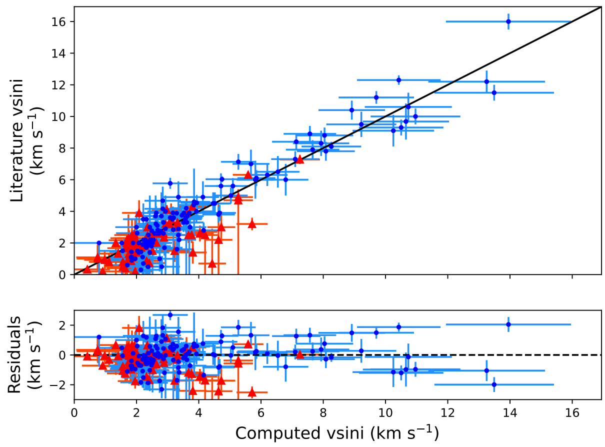

Fig. 8. Comparison between $v_{eq} \sin i_\star$ values from the literature (y-axis) and estimated from the CCF $FWHM_{DRS}$ (x-axis). Upper panel: blue dots are values computed with the G2 mask relation, and red triangles are those computed with the K5 mask relation. The black line shows the one-to-one correlation. Lower panel: residuals of the one-to-one correlation shown above.

As it is shown in Fig. 9, there is almost no difference between the relation obtained using the whole literature data set and the original one obtained from the selected calibrators (Table 1) for the G2 mask, while the situation is different when using the K5 mask (see the black solid line and red dashed line in Fig. 10). In this case, the spread is larger (and the Spearman's r coefficient lower), and so is the difference between the original calibration and the new one. We also lack reliable data points with $FWHM_{DRS} > 12$ km s^{-1}, and the literature $v_{eq} \sin i_\star$ values are very spread out. The latter fact could be caused by the type of stars that are usually reduced using the K5 mask, that is mid and late K-type and early M-type stars: these objects may be very active and this could affect both the shape of the CCF (and thus the $FWHM_{DRS}$) and the $v_{eq} \sin i_\star$ estimation performed in the literature. To better investigate this behaviour, and to check the possible limitations of our relations' applicability range, we looked at the sample considering also the stellar parameters of the stars, that is T_{eff}, $\log g$, and [Fe/H]. We recovered the parameters from SIMBAD[6] (Wenger et al. 2000) using an automated python query. We show the results in Fig. 11 for the G2 relation, and in Fig. 12 for the K5 relation. While there is no obvious trend in looking at the results from the G2 relation, we can see that stars with $\log g < 3.5$ tend to cluster below the one-to-one correlation when comparing the results from the K5 relation to the literature $v_{eq} \sin i_\star$ values. If we perform a linear fit between our $v_{eq} \sin i_\star$ and the literature $v_{eq} \sin i_\star$ only for stars with $\log g > 3.5$ (blue dotted line in Fig. 10), then the resulting relation agrees much better with that obtained from the selected calibrators:

$$\text{K5 mask}: v_{eq} \sin i_\star = 1.34470 \times FWHM_{DRS} - 6.69438. \quad (15)$$

While we advise using Eq. (7) to compute $v_{eq} \sin i_\star$ because we trust our selected calibrators better, in Table 2 we also list the parameters' errors and correlation factors needed to compute the errors when using Eq. (14) (G2 mask only) and Eq. (15) (K5 mask).

We can assume that, at least in the case of the K5 sample, our relations are applicable only for stars with $\log g > 3.5$, that is mostly main sequence stars, but also some subgiant and red giant stars may fall in the applicability range. Unfortunately, we do not have a wide enough range of $\log g$ values in our G2 sample to test

[6] http://simbad.u-strasbg.fr/simbad/

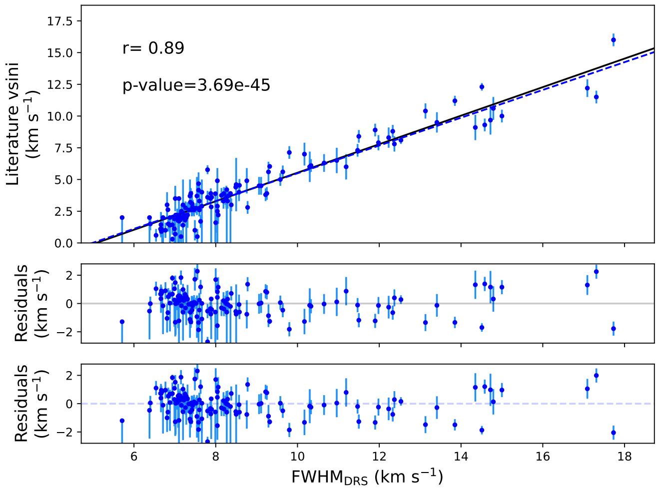

Fig. 9. Comparison between the G2 FWHM$_{\rm DRS}$ and the literature $v_{\rm eq} \sin i_\star$ values. Upper panel: correlation between the G2 FWHM$_{\rm DRS}$ (x-axis) and the literature $v_{\rm eq} \sin i_\star$ values (y-axis), with the Spearman's correlation coefficient r and p-value shown in the plot. The black line shows the linear fit of the data, and the blue dashed line shows the relation obtained from our selected calibrators (Eq. (7)). Middle panel: residuals of the linear fitting. Lower panel: residuals of the relation from selected calibrators.

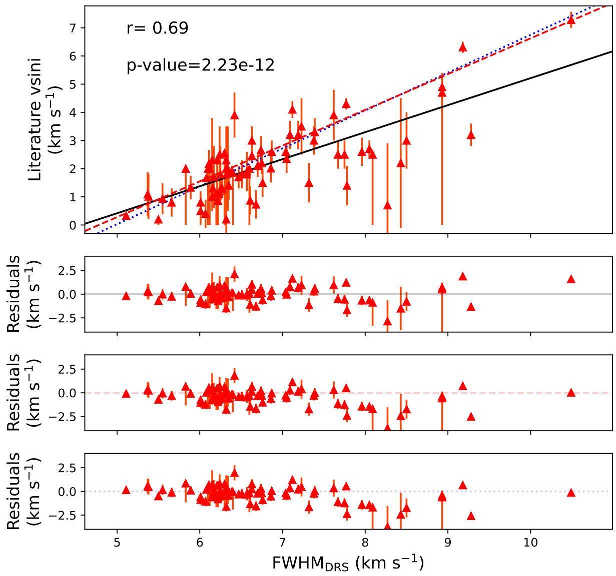

Fig. 10. Comparison between the K5 FWHM$_{\rm DRS}$ and the literature $v_{\rm eq} \sin i_\star$ values. Upper panel: correlation between the K5 FWHM$_{\rm DRS}$ (x-axis) and the literature $v_{\rm eq} \sin i_\star$ values (y-axis), with the Spearman's correlation coefficient r and p-value shown in the plot. The black line shows the linear fit of the data, the red dashed line shows the relation obtained from our selected calibrators (Eq. (7)), and the blue dotted line shows the linear fit after removing the stars with $\log g < 3.5$. Lower panels: residuals of the linear fitting, the relation from selected calibrators, and the linear fitting after removing the stars with $\log g < 3.5$.

the same behaviour (see Fig. 11, middle panel); however, considering that the G2 mask used in the HARPS-N DRS is optimized for the Sun, we can infer that also the G2 relation is best suited for main-sequence stars.

Comparing our results with the literature $v_{\rm eq} \sin i_\star$, we found no stars where our $v_{\rm eq} \sin i_\star$ differs more the 3σ from the literature value, and only four where the difference is larger than 2σ (WASP-1, WASP-127, TYC 1422-614-1, and TYC 3667-1280-1).

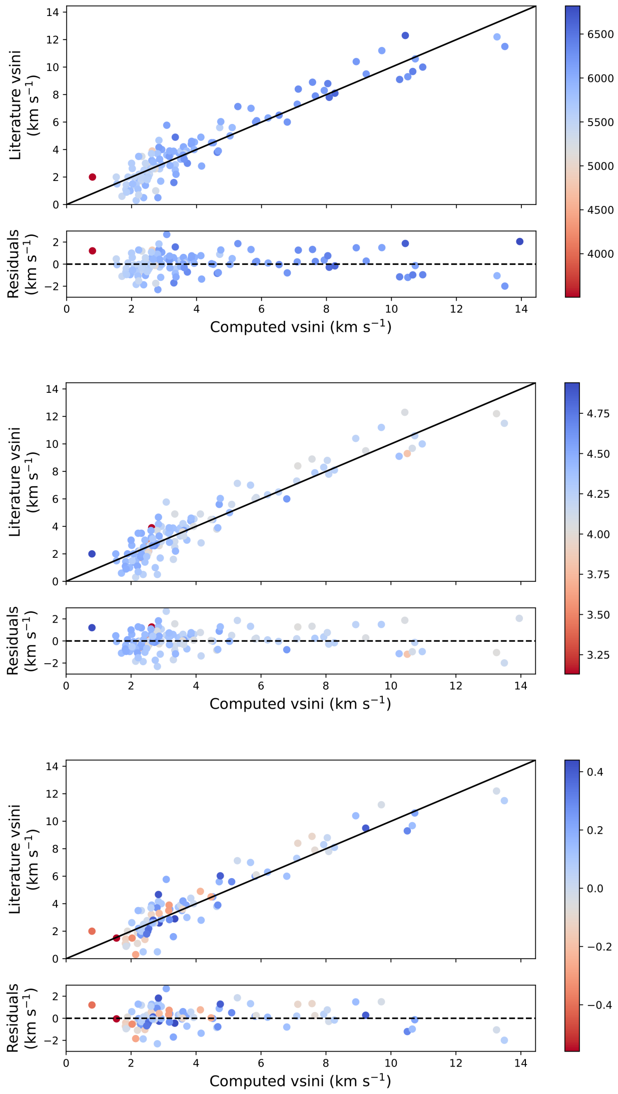

Fig. 11. Comparison between our $v_{\rm eq} \sin i_\star$ (x-axis) and the literature values (y-axis) when using the G2 relation, colour-coded according to the stellar parameters $T_{\rm eff}$ (upper panel), $\log g$ (middle panel), and [Fe/H] (lower panel).

Taking into account the very different methods used in literature to compute $v_{\rm eq} \sin i_\star$, this is a good indicator of the robustness and reliability of our FWHM$_{\rm DRS}$-$v_{\rm eq} \sin i_\star$ relation.

4.2. Stellar inclination

We focussed on the results we obtained for stars with no $v_{\rm eq} \sin i_\star$ literature value to see if we were able to recover an estimate of the stellar inclination $i_\star$. We did not perform this work on the other targets because our results do not differ much from those already in the literature, and so we do not expect any substantial changes or improvements on $i_\star$.

We used Eq. (1) to compute $i_\star$, which means that we could only work with objects with known $P_{\rm rot}$ and $R_\star$. In some cases, the exoplanetary orbit inclination was known: we could then compare it to $i_\star$, so as to check the spin-orbit alignment of the system. Because of the sometimes large errors on the various parameters, many $i_\star$ results were compatible with the whole range of possible inclinations.

We show in Table 5 only the results that set some constrains on the stellar possible inclination. While in most cases our results

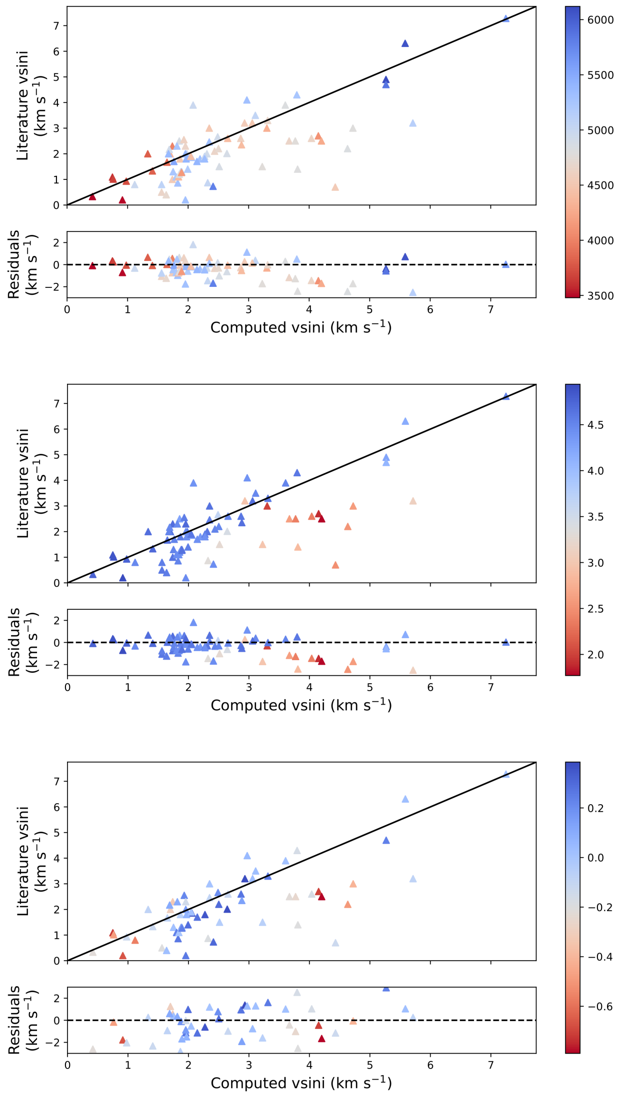

Fig. 12. Comparison between our $v_{\rm eq} \sin i_\star$ (x-axis) and the literature values (y-axis) when using the K5 relation, colour-coded according to the stellar parameters $T_{\rm eff}$ (upper panel), $\log g$ (middle panel), and [Fe/H] (lower panel).

are compatible with aligned, edge-on planetary systems, we still found one system that shows a difference between $i_\star$ and i_p around the 2σ level (K2-173), and another (HD 13931) where the $i_\star$ and i_p values point to a possibly aligned, but not edge-on system.

5. Extension to other spectrographs

The relations found in our work between $\mathrm{FWHM_{DRS}}$ and $v_{\rm eq} \sin i_\star$ are optimized for a specific combination of instruments, software, and stellar masks. While there are other spectrographs with dedicated DRS, and a few of them also deliver the spectra's CCFs as output, the different resolution, instrumental effects, wavelength ranges, numerical codes used to compute the CCF, and stellar masks could heavily influence the $\mathrm{FWHM_{DRS}}$–$v_{\rm eq} \sin i_\star$ relation. A possible exception could be the HARPS spectrograph (Mayor et al. 2003), of which HARPS-N is a twin, not only concerning the hardware, but also the software, as HARPS and HARPS-N have almost the same DRS.

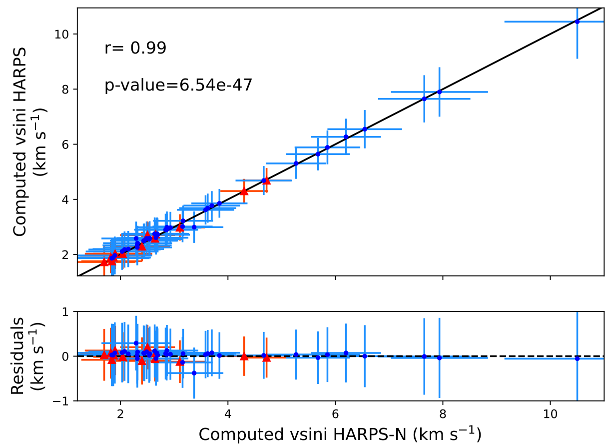

Fig. 13. Comparison between $v_{\rm eq} \sin i_\star$ computed from the HARPS-N $\mathrm{FWHM_{DRS}}$ (x-axis) and those computed from the HARPS $\mathrm{FWHM_{DRS}}$ (y-axis). Upper panel: the blue dots are the values computed with the G2 mask relation, and the red triangles are those computed with the K5 mask relation. The black line shows the one-to-one correlation. Lower panel: residuals.

To test this assumption, we checked the public archives of two spectrographs with a similar spectral range as HARPS-N: HARPS (which also has the same resolution, telescope aperture, and DRS as HARPS-N) and SOPHIE[7]. Both spectrographs have been used for many years in the exoplanets' search and characterization field, guaranteeing the availability of a large amount of public data of exoplanet-host stars. The main characteristics of HARPS-N, HARPS, and SOPHIE are listed in Table 6. SOPHIE has a HR and a high-efficiency (HE) mode, but for a more direct comparison with HARPS-N we focussed on the HR mode spectra to start. Both HARPS and SOPHIE have dedicated DRS that deliver the spectra's CCFs and their FWHMs using stellar masks similar (or, in the case of HARPS, identical) to the HARPS-N ones. We note here that also SOPHIE DRS is adapted from the HARPS DRS, so the three instruments have the same or a very similar DRS.

We searched the dedicated HARPS[8] and SOPHIE[9] archives for objects listed in Table 4 to download their HARPS and SOPHIE CCFs. We selected only the CCFs obtained with either the G2 or K5 mask in HR mode, up to a maximum of 50 per object, so that, when possible, we could recover a statistically robust median $\mathrm{FWHM_{DRS}}$ for each object. We then computed the $v_{\rm eq} \sin i_\star$ from the median $\mathrm{FWHM_{DRS}}$ using Eq. (7), and we compared the results with our HARPS-N $v_{\rm eq} \sin i_\star$. Figure 13 shows the comparison between the HARPS-N and HARPS results, and Fig. 14 shows the comparison between the HARPS-N and SOPHIE results.

It is plainly visible that the twin status of the HARPS and HARPS-N spectrographs would allow us to use the HARPS-N calibration directly with the HARPS data. It is interesting to note that because we used HARPS spectra observed both before and after 2015, this is true for HARPS data taken both before and after the change of fibres (Lo Curto et al. 2015), even if this change should have slightly affected the $\mathrm{FWHM_{DRS}}$.

The situation regarding the SOPHIE data is slightly different: applying the HARPS-N relation to the SOPHIE data results in $v_{\rm eq} \sin i_\star$ values consistently overestimated, in particular at the

[7] http://www.obs-hp.fr/guide/sophie/sophie-eng.shtml
[8] http://archive.eso.org/scienceportal/home
[9] http://atlas.obs-hp.fr/sophie/

Table 5. Stellar inclination $i_\star$ derived from our $v_{\rm eq}\sin i_\star$ values, compared with the planetary orbit inclination i_p, if known.

Name	$P_{\rm rot}$ [days]	$R_\star$ [$R_\odot$]	$v_{\rm eq}\sin i_\star$ [km s^{-1}]	$i_\star$ [deg]	i_p [deg]
GJ 328	33.6 [a]	0.65±0.02 [a]	1.55±0.60 [b]	>75 [b]	–
HD 13931	26 [c]	1.23±0.06 [c]	2.41±0.63 [b]	>47 [b]	39^{+13}_{-8} planet b [d]
HD 26965	37–43 [e]	0.87±0.17 [f]	1.44±0.61 [b]	>40 [b]	–
K2-3	40±2 [g]	0.561±0.068 [h]	1.21±0.63 [b]	>52 [b]	$89.588^{+0.116}_{-0.100}$ planet b [g]
K2-79	29.08±6.20 [i]	$1.247^{+0.077}_{-0.072}$ [j]	2.46±0.63 [b]	>48 [b]	$88.63^{+0.98}_{-1.66}$ [j] planet b
K2-155	34.8±8.2 [j]	$0.58^{+0.06}_{-0.03}$ [k]	1.20±0.63 [b]	>36 [b]	$88.3^{+1.2}_{-1.9}$ planet b [k]
					$88.96^{+0.71}_{-0.88}$ planet c [k]
					$89.61^{+0.27}_{-0.48}$ planet d [k]
K2-173	20.31±2.12 [i]	1.00±0.08 [l]	1.58±0.74 [b]	39±23 [b]	$87.83^{+1.54}_{-2.87}$ planet b [i]
K2-198	6.97±0.41 [i]	$0.78^{+0.03}_{-0.05}$ [l]	5.48±0.48 [b]	75^{+15}_{-27} [b]	$88.904^{+0.094}_{-0.027}$ planet b [m]
					$86.494^{+0.268}_{-0.088}$ planet c [m]
					$86.494^{+0.268}_{-0.088}$ planet d [m]
Kepler-495	19.20±2.98 [n]	$0.867^{+0.039}_{-0.037}$ [o]	1.76±0.71 [b]	50±30 [b]	–
Kepler-849	17.91±0.48 [n]	$1.828^{+0.086}_{-0.081}$ [o]	4.58±0.52 [b]	62±14 [b]	–
Kepler-1514	7.83±0.16 [n]	$1.273^{+0.055}_{-0.052}$ [o]	7.79±0.88 [b]	72^{+18}_{-21} [b]	$89.944^{+0.013}_{-0.010}$ planet b [p]
					$87.98^{+1.20}_{-0.40}$ planet c [p]
WASP-85 A	15.1±0.6 [q]	0.935±0.023 [q]	2.72±0.60 [b]	60±22 [b]	$89.69^{+0.11}_{-0.03}$ planet b [q]

References. [a]Küker et al. (2019); [b]this work; [c]Howard et al. (2010); [d]Philipot et al. (2023); [e]Díaz et al. (2018); [f]Ma et al. (2018); [g]Kosiarek et al. (2019); [h]Crossfield et al. (2015); [i]Reinhold & Hekker (2020); [j]Mayo et al. (2018); [k]Díez Alonso et al. (2018); [l]Stassun et al. (2019); [m]Hedges et al. (2019); [n]Mazeh et al. (2015); [o]Berger et al. (2018); [p]Dalba et al. (2021); [q]Močnik et al. (2016).

Table 6. Main characteristics of the HARPS-N, HARPS, and SOPHIE spectrographs.

Spectrograph	Telescope diameter [m]	Wavelength range [nm]	Resolution
HARPS-N	3.58	385–691	115 000
HARPS	3.57	378–691	115 000
SOPHIE (HR)	1.93	387–694	75 000
SOPHIE (HE)	1.93	387–694	40 000

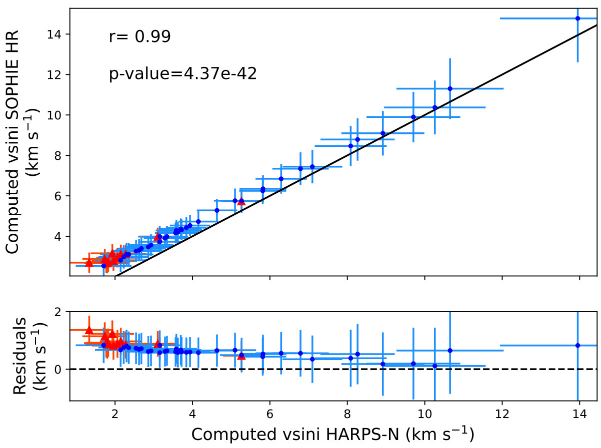

Fig. 14. Comparison between $v_{\rm eq}\sin i_\star$ computed from the HARPS-N FWHM$_{\rm DRS}$ (x-axis) and those computed from the SOPHIE HR FWHM$_{\rm DRS}$ (y-axis). Upper panel: the blue dots are the values computed with the G2 mask relation, and the red triangles are those computed with the K5 mask relation. The black line shows the one-to-one correlation. Lower panel: residuals.

lower end of the range. This is not surprising since the lower resolution of SOPHIE as compared to HARPS-N result in larger FWHM$_{\rm DRS}$ values due to the greater instrumental broadening. Still, the effect is not simply a rigid shift, but it appears as a parabolic trend. We manipulated the SOPHIE FWHM$_{\rm DRS}$ values in order to correct them for the different instrumental resolution, using the following equation:

$$FWHM_{\rm new} = \sqrt{FWHM^2_{\rm DRS} - \left(\frac{c}{R_{\rm SOPHIE}}\right)^2 + \left(\frac{c}{R_{\rm HARPS-N}}\right)^2}, \tag{16}$$

where c is the speed of light in km s^{-1}, and $R_{\rm SOPHIE}$ and $R_{\rm HARPS-N}$ are the resolution of SOPHIE and HARPS-N, respectively (see Table 6). The $v_{\rm eq}\sin i_\star$ values computed with FWHM$_{\rm new}$ are in much better agreement with those derived from HARPS-N data, as shown in Fig. 15. While the spread between HARPS-N and SOPHIE $v_{\rm eq}\sin i_\star$ values is a bit larger than that between the HARPS-N and HARPS ones, it still seems that our relation could also be used with the SOPHIE data, once they are corrected for the difference in resolution.

To better test this assumption, we also selected the SOPHIE CCFs computed from the spectra observed in the HE mode and then we compared the $v_{\rm eq}\sin i_\star$ computed from both the FWHM$_{\rm DRS}$ and FWHM$_{\rm new}$. The FWHM$_{\rm new}$ values were derived using Eq. (16) with the HE resolution. The results are shown in Fig. 16: while correcting for the resolution does improve the agreement between HARPS-N and SOPHIE HE $v_{\rm eq}\sin i_\star$ values, the results are still discrepant. It seems then that a simple correction for the different resolutions is not enough to adapt our relation to a different spectrograph, at least when the resolution difference is large enough. This assumes that there are not any other factors at play, such as a difference in the code to compute HR and HE CCFs in the SOPHIE DRS.

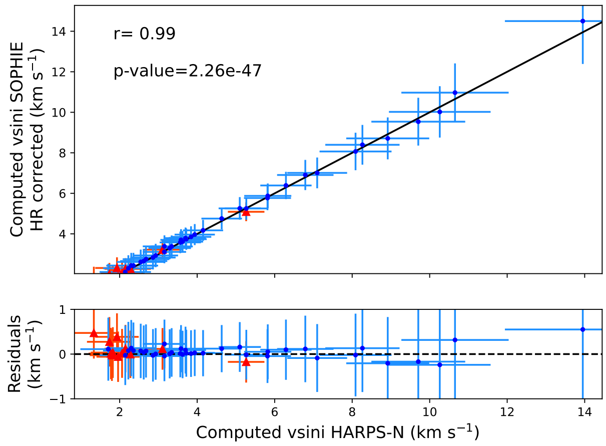

Fig. 15. Comparison between $v_{eq} \sin i_\star$ computed from the HARPS-N $FWHM_{DRS}$ (x-axis) and those computed from the corrected SOPHIE HR $FWHM_{new}$ (y-axis). Upper panel: the blue dots are the values computed with the G2 mask relation, and the red triangles are those computed with the K5 mask relation. The black line shows the one-to-one correlation. Lower panel: residuals.

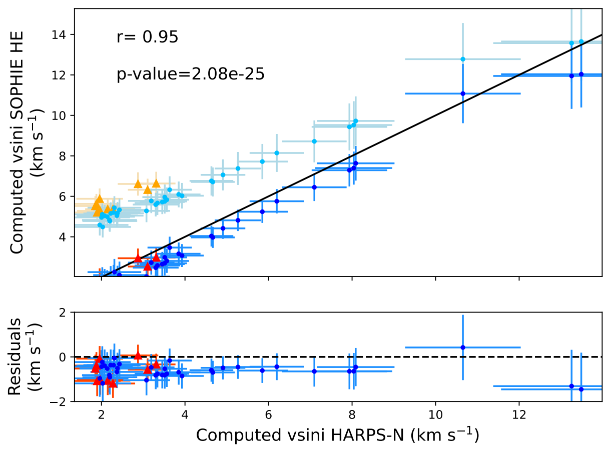

Fig. 16. Comparison between $v_{eq} \sin i_\star$ computed from the HARPS-N $FWHM_{DRS}$ (x-axis) and those computed with SOPHIE in HE mode (y-axis). Upper panel: orange triangles and light blue dots are the results from SOPHIE HE $FWHM_{DRS}$ with the K5 and G2 relation, respectively, while the red triangles and blue dots are the results from the corrected SOPHIE HE $FWHM_{new}$ (y-axis). The black line shows the one-to-one correlation. Lower panel: residuals for the corrected SOPHIE HE $FWHM_{new}$ only.

Unfortunately, we cannot test our method further on any other instrument because very few spectrographs are equipped with dedicated DRS that also yield the CCFs in addition to the reduced spectra. ESPRESSO has the same capabilities (and a DRS derived from the HARPS one), but there are not enough public data from this instrument for a meaningful comparison. We were unable to compare the HARPS-N results with those obtained with instruments with a very different spectral coverage (such as the visible and near-infrared spectrograph CARMENES or the near-infrared spectrograph GIANO-B), because their DRSs do not compute any CCFs.

Still, in case any other future DRS will also yield the CCFs, it will be of fundamental importance to calibrate or check and adapt this relation for each combination of instruments, wavelength range, spectral resolution, mathematical recipe (to compute both the CCF and FWHM), and stellar mask. While the work is quite straightforward in the case of instruments such as HARPS-N (which offers a single, fixed choice of wavelength coverage and resolution), it may become slightly more complex when applied to instruments such as ESPRESSO (with three different resolving powers) or UVES (where a wide range of choices in both wavelength coverage and spectral resolution is available). In any case, the strategy detailed in this paper in order to calibrate a $FWHM_{DRS}$–$v_{eq} \sin i_\star$ relation may be applied to any other relevant cases including self-made codes, allowing for the information carried in the CCFs to be better exploited.

6. Conclusions

Using a well-defined set of calibrators, we were able to obtain two straightforward relations to obtain an estimation of the stellar $v_{eq} \sin i_\star$ directly from the $FWHM_{DRS}$ computed by the HARPS-N DRS using the G2 and K5 masks (see Eq. (7)). These calibrations may be applied when the $FWHM_{DRS}$ value is less than 20 km s^{-1}. For larger values, other methods to compute the $v_{eq} \sin i_\star$ are more accurate (i.e. Fourier transform or rotational profile fitting). Other relations were computed to be used when it is possible to estimate v_{micro} and/or v_{macro}, and thus remove their contribution to the $FWHM_{DRS}$.

We applied our basic relations to all the exoplanet-host stars found in the HARPS-N public archive and in the GAPS private data with CCFs computed with the G2 or K5 mask and $FWHM_{DRS} < 20$ km s^{-1}: we obtained a catalogue of homogeneous $v_{eq} \sin i_\star$ measurements for 273 exoplanet-host stars. Of these stars, 206 have literature values of $v_{eq} \sin i_\star$: comparing our results with those, we found a very good agreement, with no object differing more than 3σ. Considering the stellar parameters when comparing our results with the literature, we constrained our relation to stars with $\log g > 3.5$.

We can reliably affirm that our simple $FWHM_{DRS}$-$v_{eq} \sin i_\star$ relations give solid results, comparable with those obtained with more sophisticated methods such as spectral synthesis. While our errors may overall be larger than those obtained in the literature, our results would still be useful in characterizing exoplanetary properties, and they may be used as a starting point for a more detailed analysis of the exoplanetary systems. In fact, we were able to determine or constrain the stellar inclination for 12 exoplanet-host stars with no previous $v_{eq} \sin i_\star$ measurements, finding hints of spin-orbit misalignment in the K2-173 system.

We also tested our relations on the $FWHM_{DRS}$ computed by the HARPS and SOPHIE DRS, and we conclude that Eq. (7) may be used as it is also with HARPS data taken in high accuracy mode (R = 115 000). It would be possible to use our relation on the SOPHIE HR data once they are corrected for the different resolution, while using the SOPHIE HE data would require some additional fine-tuning. Still, the strategy detailed in this paper (selection of the calibration, creation of the $FWHM_{DRS}$-$v_{eq} \sin i_\star$ relation, test of the applicability range) may be used to calibrate other $FWHM_{DRS}$-$v_{eq} \sin i_\star$, with different combinations of instrument resolutions, wavelength ranges, mathematical codes (to compute both the CCF and FWHM), and stellar masks.

Acknowledgements. This paper is based on observations collected with the 3.58 m Telescopio Nazionale *Galileo* (TNG), operated on the island of La Palma (Spain) by the Fundación Galileo Galilei of the INAF (Istituto Nazionale di Astrofisica) at the Spanish Observatorio del Roque de los Muchachos, in the frame of the programme Global Architecture of Planetary Systems (GAPS). This research used the facilities of the Italian Center for Astronomical Archive (IA2) operated by INAF at the Astronomical Observatory of Trieste. This research has made use of the SIMBAD database, operated at CDS, Strasbourg, France L. M. acknowledges support from the "Fondi di Ricerca Scientifica d'Ateneo

2021" of the University of Rome "Tor Vergata". G.S. acknowledges support from CHEOPS ASI-INAF agreement n. 2019-29-HH.0.

References

Adibekyan, V. Z., Delgado Mena, E., Sousa, S. G., et al. 2012, A&A, 547, A36
Anderson, D. R., Collier Cameron, A., Delrez, L., et al. 2014, MNRAS, 445, 1114
Bakos, G. Á., Hartman, J., Torres, G., et al. 2011, ApJ, 742, 116
Baranne, A., Queloz, D., Mayor, M., et al. 1996, A&AS, 119, 373
Benomar, O., Masuda, K., Shibahashi, H., & Suto, Y. 2014, PASJ, 66, 94
Berger, T. A., Huber, D., Gaidos, E., & van Saders, J. L. 2018, ApJ, 866, 99
Biazzo, K., D'Orazi, V., Desidera, S., et al. 2022, A&A, 664, A161
Bonomo, A. S., Desidera, S., Benatti, S., et al. 2017, A&A, 602, A107
Boyajian, T., von Braun, K., Feiden, G. A., et al. 2014, MNRAS, 447, 846
Brewer, J. M., Fischer, D. A., Valenti, J. A., & Piskunov, N. 2016, ApJS, 225, 41
Buchhave, L. A., Bakos, G. Á., Hartman, J. D., et al. 2010, ApJ, 720, 1118
Butler, R. P., Marcy, G. W., Williams, E., Hauser, H., & Shirts, P. 1997, ApJ, 474, L115
Butters, O. W., West, R. G., Anderson, D. R., et al. 2010, A&A, 520, L10
Choi, J., Dotter, A., Conroy, C., et al. 2016, ApJ, 823, 102
Collins, K. A., Kielkopf, J. F., & Stassun, K. G. 2017, AJ, 153, 78
Cosentino, R., Lovis, C., Pepe, F., et al. 2014, Proc. SPIE, 9147, 91478C
Covino, E., Esposito, M., Barbieri, M., et al. 2013, A&A, 554, A28
Crossfield, I. J. M., Petigura, E., Schlieder, J. E., et al. 2015, ApJ, 804, 10
Crouzet, N., McCullough, P. R., Burke, C., & Long, D. 2012, ApJ, 761, 7
Dalba, P. A., Kane, S. R., Isaacson, H., et al. 2021, AJ, 161, 103
Díaz, M. R., Jenkins, J. S., Tuomi, M., et al. 2018, AJ, 155, 126
Díez Alonso, E., Suárez Gómez, S. L., González Hernández, J. I., et al. 2018, MNRAS, 476, L50
Dotter, A. 2016, ApJS, 222, 8
Doyle, A. P., Davies, G. R., Smalley, B., Chaplin, W. J., & Elsworth, Y. 2014, MNRAS, 444, 3592
Eastman, J. D., Rodriguez, J. E., Agol, E., et al. 2019, ArXiv e-prints [arXiv:1907.09480]
Esposito, M., Covino, E., Desidera, S., et al. 2017, A&A, 601, A53
Fischer, D. A., Vogt, S. S., Marcy, G. W., et al. 2007, ApJ, 669, 1336
Gaia Collaboration (Prusti, T., et al.) 2016, A&A, 595, A1
Gaia Collaboration (Brown, A. G. A., et al.) 2021, A&A, 649, A1
Gray, D. F. 2008, The Observation and Analysis of Stellar Photospheres (Cambridge: Cambridge University Press)
Hedges, C., Saunders, N., Barentsen, G., et al. 2019, ApJ, 880, L5
Hellier, C., Anderson, D. R., Collier Cameron, A., et al. 2011, A&A, 535, L7
Hirano, T., Sanchis-Ojeda, R., Takeda, Y., et al. 2014, ApJ, 783, 9
Horne, J. H., & Baliunas, S. L. 1986, ApJ, 302, 757
Howard, A. W., Johnson, J. A., Marcy, G. W., et al. 2010, ApJ, 721, 1467
Hunter, A. A., Macgregor, A. B., Szabo, T. O., et al. 2012, Source Code Biol. Med., 7, 1
Johnson, J. A., Payne, M., Howard, A. W., et al. 2011, AJ, 141, 16
Kosiarek, M. R., Crossfield, I. J. M., Hardegree-Ullman, K. K., et al. 2019, AJ, 157, 97
Küker, M., Rüdiger, G., Olah, K., & Strassmeier, K. G. 2019, A&A, 622, A40
Lamm, M. H., Bailer-Jones, C. A. L., Mundt, R., Herbst, W., & Scholz, A. 2004, A&A, 417, 557
Livingston, J. H., Crossfield, I. J. M., Petigura, E. A., et al. 2018, AJ, 156, 277
Lo Curto, G., Pepe, F., Avila, G., et al. 2015, The Messenger, 162, 9
Ma, B., Ge, J., Muterspaugh, M., et al. 2018, MNRAS, 480, 2411
Mancini, L., Southworth, J., Ciceri, S., et al. 2014, MNRAS, 443, 2391
Mancini, L., Esposito, M., Covino, E., et al. 2018, A&A, 613, A41
Mann, A. W., Johnson, M. C., Vanderburg, A., et al. 2020, AJ, 160, 179
Mayo, A. W., Vanderburg, A., Latham, D. W., et al. 2018, AJ, 155, 136
Mayor, M., & Queloz, D. 1995, Nature, 378, 355
Mayor, M., Pepe, F., Queloz, D., et al. 2003, The Messenger, 114, 20
Mazeh, T., Perets, H. B., McQuillan, A., & Goldstein, E. S. 2015, ApJ, 801, 3
McLaughlin, D. B. 1924, ApJ, 60, 22
McQuillan, A., Mazeh, T., & Aigrain, S. 2013, ApJ, 775, L11
Ment, K., Fischer, D. A., Bakos, G., Howard, A. W., & Isaacson, H. 2018, AJ, 156, 213
Močnik, T., Clark, B. J. M., Anderson, D. R., Hellier, C., & Brown, D. J. A. 2016, AJ, 151, 150
Močnik, T., Southworth, J., & Hellier, C. 2017, MNRAS, 471, 394
Nikolov, N., Sing, D. K., Pont, F., et al. 2014, MNRAS, 437, 46
Nordström, B., Mayor, M., Andersen, J., et al. 2004, A&A, 418, 989
Nutzman, P., Gilliland, R. L., McCullough, P. R., et al. 2010, ApJ, 726, 3
Pepe, F., Mayor, M., Galland, F., et al. 2002, A&A, 388, 632
Philipot, F., Lagrange, A. M., Rubini, P., Kiefer, F., & Chomez, A. 2023, A&A, 670, A65
Queloz, D., Eggenberger, A., Mayor, M., et al. 2000, A&A, 359, L13
Rainer, M., Borsa, F., & Affer, L. 2020, Exp. Astron., 49, 73
Reinhold, T., & Hekker, S. 2020, A&A, 635, A43
Ricker, G. R., Winn, J. N., Vanderspek, R., et al. 2015, J. Astron. Teles. Instrum. Syst., 1, 014003
Roberts, D. H., Lehar, J., & Dreher, J. W. 1987, AJ, 93, 968
Rossiter, R. A. 1924, ApJ, 60, 15
Sada, P. V., & Ramón-Fox, F. G. 2016, PASP, 128, 024402
Santerne, A., Hébrard, G., Lillo-Box, J., et al. 2016, ApJ, 824, 55
Southworth, J. 2011, MNRAS, 417, 2166
Southworth, J. 2012, MNRAS, 426, 1291
Stassun, K. G., Collins, K. A., & Gaudi, B. S. 2017, AJ, 153, 136
Stassun, K. G., Oelkers, R. J., Paegert, M., et al. 2019, AJ, 158, 138
Stumpe, M. C., Smith, J. C., Van Cleve, J. E., et al. 2012, PASP, 124, 985
Villaver, E., Niedzielski, A., Wolszczan, A., et al. 2017, A&A, 606, A38
Wenger, M., Ochsenbein, F., Egret, D., et al. 2000, A&AS, 143, 9
Winn, J. N., Noyes, R. W., Holman, M. J., et al. 2005, ApJ, 631, 1215
Zechmeister, M., & Kürster, M. 2009, A&A, 496, 577

[1] INAF – Osservatorio Astronomico di Brera, Via E. Bianchi, 46, 23807 Merate (LC), Italy
e-mail: monica.rainer@inaf.it
[2] INAF – Osservatorio Astronomico di Padova, Vicolo dell'Osservatorio, 5, 35122 Padova (PD), Italy
[3] INAF – Osservatorio Astrofisico di Torino, Via Osservatorio 20, 10025 Pino Torinese (TO), Italy
[4] Department of Astronomy, University of Geneva, Chemin Pegasi 51, 1290 Versoix, Switzerland
[5] INAF – Osservatorio Astronomico di Roma, Via Frascati 33, 00078 Monte Porzio Catone (Roma), Italy
[6] INAF – Osservatorio Astrofisico di Catania, Via S.Sofia 78, 95123 Catania, Italy
[7] INAF – Osservatorio Astronomico di Palermo, Piazza del Parlamento, 1, 90134 Palermo, Italy
[8] Instituto de Astrofísica de Canarias (IAC), 38205 La Laguna, Tenerife, Spain
[9] INAF – Osservatorio Astronomico di Capodimonte, via Moiariello 16, 80131 Napoli, Italy
[10] Université Côte d'Azur, Observatoire de la Côte d'Azur, CNRS, Laboratoire Lagrange, Bd de l'Observatoire, CS34229, 06304 Nice Cedex 4, France
[11] Department of Physics, University of Rome "Tor Vergata", Via della Ricerca Scientifica 1, 00133 Rome, Italy
[12] Max Planck Institute for Astronomy, Königstuhl 17, 69117 Heidelberg, Germany
[13] Aix Marseille Univ, CNRS, CNES, LAM, Marseille, France
[14] INAF – Osservatorio Astronomico di Trieste, via Tiepolo 11, 34143 Trieste, Italy
[15] INAF – Fundación Galileo Galilei, Rambla José Ana Fernandez Pérez 7, 38712 Breña Baja (TF), Spain
[16] INAF – Osservatorio Astronomico di Cagliari, via della Scienza 5, 09047 Selargius (CA), Italy